FINAL REPORT

BDV30 977 — 03

Evaluation of Fog Predictions and Detection

Peter S. Ray. Ph.D.
Daphne Lefran

Florida State University
Department of Earth, Ocean, and Atmospheric Science
Meteorology Program
Tallahassee, Florida 32306

March 2015

DISCLAIMER

"The opinions, findings, and conclusions expressed in this publication are those of the authors and not necessarily those of the State of Florida Department of Transportation."

SI* (MODERN METRIC) Conversion Factors

APPROXIMATE CONVERSIONS TO SI UNITS

SYMBOL	WHEN YOU KNOW	MULTIPLY BY	TO FIND	SYMBOL
LENGTH				
in	inches	25.4	millimeters	mm
ft	feet	0.305	meters	m
yd	yards	0.914	meters	m
mi	miles	1.61	kilometers	km

SYMBOL	WHEN YOU KNOW	MULTIPLY BY	TO FIND	SYMBOL
AREA				
in^2	squareinches	645.2	square millimeters	mm^2
ft^2	squarefeet	0.093	square meters	m^2
yd^2	square yard	0.836	square meters	m^2
ac	acres	0.405	hectares	ha
mi^2	square miles	2.59	square kilometers	km^2

SYMBOL	WHEN YOU KNOW	MULTIPLY BY	TO FIND	SYMBOL
VOLUME				
fl oz	fluid ounces	29.57	milliliters	mL
gal	gallons	3.785	liters	L
ft^3	cubic feet	0.028	cubic meters	m^3
yd^3	cubic yards	0.765	cubic meters	m^3
NOTE: volumes greater than 1000 L shall be shown in m^3				

SYMBOL	WHEN YOU KNOW	MULTIPLY BY	TO FIND	SYMBOL
MASS				
oz	ounces	28.35	grams	g
lb	pounds	0.454	kilograms	kg
T	short tons (2000 lb)	0.907	megagrams (or "metric ton")	Mg (or "t")

SYMBOL	WHEN YOU KNOW	MULTIPLY BY	TO FIND	SYMBOL
TEMPERATURE (exact degrees)				
^{o}F	Fahrenheit	5 (F-32)/9 or (F-32)/1.8	Celsius	^{o}C

SYMBOL	WHEN YOU KNOW	MULTIPLY BY	TO FIND	SYMBOL
ILLUMINATION				
fc	foot-candles	10.76	lux	lx
fl	foot-Lamberts	3.426	candela/m^2	cd/m^2

SYMBOL	WHEN YOU KNOW	MULTIPLY BY	TO FIND	SYMBOL
FORCE and PRESSURE or STRESS				
lbf	poundforce	4.45	newtons	N
lbf/in^2	poundforce per square inch	6.89	kilopascals	kPa

APPROXIMATE CONVERSIONS TO SI UNITS

SYMBOL	WHEN YOU KNOW	MULTIPLY BY	TO FIND	SYMBOL
LENGTH				
mm	millimeters	0.039	inches	in
m	meters	3.28	feet	ft
m	meters	1.09	yards	yd
km	kilometers	0.621	miles	mi

SYMBOL	WHEN YOU KNOW	MULTIPLY BY	TO FIND	SYMBOL
AREA				
mm^2	square millimeters	0.0016	square inches	in^2
m^2	square meters	10.764	square feet	ft^2
m^2	square meters	1.195	square yards	yd^2
ha	hectares	2.47	acres	ac
km^2	square kilometers	0.386	square miles	mi^2

SYMBOL	WHEN YOU KNOW	MULTIPLY BY	TO FIND	SYMBOL
VOLUME				
mL	milliliters	0.034	fluid ounces	fl oz
L	liters	0.264	gallons	gal
m^3	cubic meters	35.314	cubic feet	ft^3
m^3	cubic meters	1.307	cubic yards	yd^3

SYMBOL	WHEN YOU KNOW	MULTIPLY BY	TO FIND	SYMBOL
MASS				
g	grams	0.035	ounces	oz
kg	kilograms	2.202	pounds	lb
Mg (or "t")	megagrams (or "metric ton")	1.103	short tons (2000 lb)	T

SYMBOL	WHEN YOU KNOW	MULTIPLY BY	TO FIND	SYMBOL
TEMPERATURE (exact degrees)				
^{o}C	Celsius	1.8C+32	Fahrenheit	^{o}F

SYMBOL	WHEN YOU KNOW	MULTIPLY BY	TO FIND	SYMBOL
ILLUMINATION				
lx	lux	0.0929	foot-candles	fc
cd/m^2	candela/m^2	0.2919	foot-Lamberts	fl

SYMBOL	WHEN YOU KNOW	MULTIPLY BY	TO FIND	SYMBOL
FORCE and PRESSURE or STRESS				
N	newtons	0.225	poundforce	lbf
kPa	kilopascals	0.145	poundforce per square inch	lbf/in^2

*SI is the symbol for the International System of Units. Appropriate rounding should be made to comply with Section 4 of ASTM E380.
(Revised March 2003)

Technical Report Documentation Page

1. Report No. BDV30 977 — 03		3. Recipient's Catalog No.

4. Title and Subtitle **Evaluation of Fog Predictions and Detection**	5. Report Date 3/31/2015
	6. Performing Organization Code
7. Author(s) **Peter S. Ray, PhD, Daphne Lafran**	8. Performing Organization Report No.
9. Performing Organization Name and Address **Department of Earth, Ocean and Atmospheric Sciences** **Florida State University**	10. Work Unit No. (TRAIS)
	11. Contract or Grant No. BDV30 977 — 03
12. Sponsoring Agency Name and Address **Florida Department of Transportation**	13. Type of Report and Period Covered **Final Report**
	14. Sponsoring Agency Code
15. Supplementary Notes	

16. Abstract

On January 29, 2012 at about 4:00 am a thick fog and smoke caused a multiple car crash just south of Gainesville, Florida. 11 people were killed and 18 were hospitalized. Nationally there are about 38,000 fog related accidents which result in about 620 fatalities. Because of the continuous observations of all points within Florida, the data from a geostationary satellite was used in which to better anticipate the formation of fog along Florida roadways, and to identify fog when it does form. The year of 2012 was chosen to examine where fog forms and if it is possible to reliably detect fig, It was found that using the difference in two frequencies in the infrared spectrum that have difference water absorption characteristic, that it was possible to infer the presence of fog. However, many non-foggy days also got included. It is though that other discriminates, such as wind speed could reduce the false alarm rate.

17. Key Word **Fog; Satellite, Reduced Visibility, Forecasting Fog, Remote Sensing**	18. Distribution Statement

19. Security Classif. (of this report) **Unclassified**	20. Security Classif. (of this page) **Unclassified**	21. No. of Pages	22. Price

Executive Summary

Fog or fog enhanced with smoke has been shown to reduce visibility to levels where diving is unsafe. Numerous pre-dawn accidents attest to this fact. The solution is to be able to slow or redirect traffic to avoid unsafe speeds in low visibility conditions. Even more desirable would to be able to anticipate those emerging conditions.

It is impractical to have instrumentation at all the possible fog locations. Thus, some constantly vigilant mechanism would be desirable. Satellites offer such a capability. To do this, the instrument must be able to at least recognize fog from space. Low earth orbiting satellites offer the best opportunity because of their greater proximity and therefor better spatial resolution. But they are orbiting the earth and are only able to view a given location a few times in a 24 our cycle. However the geostationary (GOES) satellites can see up to a hemisphere constantly. Their drawback is that they are about 23,000 miles away so resolution is about spot about 8 km on a side. An area of fog is usually much smaller than that so the ability to detect a local foggy spot is reduced.

The method employed is to measure the upwelling radiation for two different infrared channels. The most useful is Channel 4, which is centered at 11 microns, and channel 2, which is centered at 3.9 microns. For a clear night and a given surface temperature, they will each measure the a different frequency in the Plank function resulting from the upwelling radiation, both inferring the same surface temperature. However, if there is intervening cloud layer, it will intercept, absorb and reradiate at the lower temperature of the cloud, and the signal received will be weaker. Since Channel 4 is less sensitive to the absorption by water, it will more correctly measure the surface temperature while channel 2 will typically infer a colder temperature. Often for the case of fog, this is less than two degrees Kelvin.

First the procedure had to be calibrated with know temperatures and fog conditions. From this it was determined the range of brightness temperature difference that indicated the

presence of fog. Unfortunately, many times the same brightness temperature difference was found when there was no fog.

In addition, it was found that the pixels of the two channels were not geographically co-located. This required development and implementing an algorithm of correcting channel 2 so the images and data between the channels were collocated.

These results are quantified and corrections applied which enabled fog climatology with higher resolution for the State of Florida than any previous fog climatology. However, it is shown that the next generation of imager will bring at least 8 times more resolution and has the potential of truly making an improvement in the climatology and fog forecasting from the use of satellites.

TABLE OF CONTENTS

LIST OF TABLES

LIST OF FIGURES

ACRONYMS

AMS	American Meteorological Society
AP	Airport
ASOS	Automated Surface Observing System
AVHRR	Advanced Very High Resolution Radiometer
AWOS	Automated Weather Observing System
BS	Bias Score
BTD	Brightness temperature difference
CCN	Cloud Condensation Nuclei
CH	Channel
CIMSS	Cooperative Institute for Meteorological Satellite Studies
CSI	Critical Success Index
FAA	Federal Aviation Administration
FAR	False Alarm Rate
FAWN	Florida Automated Weather Network
FDOT	Florida Department of Transportation
FFTR	Fast Fourier Transformation Resampling algorithm
FOG	Fog Operational Guidance
F/S	Fog and smoke
FSU	Florida State University
GOES	Geostationary Operational Environmental Satellite
GVAR	GOES Variable

HK	Hanssen-Kuiper skill score
IR	Infrared
JD	Julian Day
kt	Knots
LW	Long wave
MADIS	Meteorological Assimilation Data Ingest System
McIdas	Man computer Interactive Data Access System
METAR	Meteorological Terminal Aviation Routine Weather Report
MIA	Miami, Florida
MOS	Model Output Statistics
NAS	Naval Air Station
NASA	National Aeronautics and Space Administration
NCDC	National Climatic Data Center
NESDIS	National Environmental Satellite, Data, and Information Service
NOAA	National Oceanic and Atmospheric Administration
NWS	National Weather Service
PC	Percent Correct
PFD	Probability of False Detection
POD	Probability of Detection
POES	Polar Orbiting Operational Satellite
RH	Relative Humidity
SEV	Sensor Equivalent Visibility
SFWMD	South Florida Water Management District

SW	Shortwave
SZA	Solar Zenith Angle
TD	Temperature difference
TLH	Tallahassee, Florida
TPA	Tampa, Florida
UCF	University of Central Florida
USGS	United States Geological Survey
UTC	Universal Time Coordinates
VISSR	Visible Infrared Spin Scan Radiometer

CHAPTER ONE

INTRODUCTION

1.1 Motivation

On November 22, 2012, at about 8:35 a.m., a thick fog resulted in a 140-car accident near Beaumont, Texas. Remarkably, only two people died and eighty people were injured and required hospital care. On January 29, 2012, about 4:00 a.m., amidst thick fog and smoke on I-75 south of Gainesville, Florida, 11 people were killed and 18 hospitalized in a multi-car crash. Nationally, there are about 38,000 fog related car accidents each year resulting in about 620 fatalities. In Florida, between 2002 and 2009, 299 people died in vehicle crashes related to fog and smoke conditions on Florida highways. This is more than the amount of deaths in Florida caused by hurricanes and lightning combined. Fog is a cloud located near ground level. All types of fog require ubiquitous cloud condensation nuclei (CCN) and can form with a relative humidity of less than 100%. The opaqueness of fog may be substantially increased by the presence of smoke, due to the increase of CCN. Fog is both spatially and temporally variable. With observation equipment widely dispersed, the challenge is how to forecast the occurrence of fog from observations far removed from the location of fog occurrence. With the available observation data from 2006 to 2010, the location and frequency of fog was determined, thus forming a baseline fog climatology. Based on data from that study, researchers evaluated fog prediction techniques and made recommendations for improving fog-warning systems along Florida's highways (Ray et al. 2014).

The definition of fog is an observed visibility below one kilometer (or 0.65 statute mile) resulting from the presence of suspended water droplets and/or ice crystals (NOAA,

1995). According to Houghton (1985), fog generally occurs when water droplets are suspended in air that is within ten percent of saturation. Typically, there are three primary physical processes that can make unsaturated air become saturated. These include cooling the air temperature, adding moisture, and mixing air parcels with different humidities and temperatures vertically (Duynkerke, 1990). There are many other atmospheric and localized factors that can exacerbate these mechanisms such as, vegetation, horizontal and vertical winds, radiation fluxes, soil moisture, and topographic effects. However, once fog has formed, the primary mechanisms influencing further fog development and intensity are radiational cooling, gravitational droplet settling, fog microphysics, and cloud cover (Duynkerke, 1990).

1.2 Types of fog

Synoptic, dynamic, and microphysical conditions will normally control what type of fog will generally form. Willett (1928) created an all-inclusive fog classification system, later revised by Byers (1959). It comprised of 11 different types of fog, each of which was categorized by the physical processes involved and the atmospheric scenario in which the fog formed. However, most of the fog types classified by Byers (1959) are merely derivatives of the four distinct types of fog as described by Stull (1999): advection fog, upslope fog, frontal fog, and radiation fog.

This project will focus primarily on radiation fog in the state of Florida. However, for the sake of completeness, the four different fog types are defined below.

1.2.1 Advection Fog

Advection fog occurs when a warm moist air mass moves over a cool surface (AMS, 1999). The warmer air mass loses heat through conduction to the cooler surface, thus lowering the temperature to its dew point temperature (Stull, 1999). The surfaces on which advection fog can form include: cold water, cold ground, and ground covered with snow or ice. Advection fog is typically found in marine environments such as coastal areas, as water sources provide the moisture and heat necessary to facilitate this fog type. However, the natural land-breeze thermal circulation that occurs in coastal regions during the early morning hours can limit the evolvement of advection fog. Therefore, overlying synoptic wind speeds and wind directions are critical in determining whether advection fog will form. According to the U.S. Department of Transportation (1975), advection fog deepens as wind speed increases up to about 15 kt. Wind speeds much stronger than 15 kt will induce turbulence and mixing, leading to fog dissipation. Sea fog is another form of advection fog where warm air advects over cooler ocean air. Through conduction, the warm air cools to its dew point temperature (Baars et al., 2003).

Sea fog typically occurs in regions of cold ocean currents to the west of continents, such as over the northeast Pacific Ocean off the coast of California (Baars et al., 2003). Sea fog is most problematic for marine transportation, and only affects ground transportation when bridges or other roadways are over a sufficient amount of water.

Both sea and land advection fogs are often more opaque and longer lasting than radiation fog (Toth et al., 2010). This contributes to the fact that advection fog, once formed, can experience radiational cooling on the top of the fog layer (Stull, 1999). This exacerbates the rate of cooling in the warm-moist air mass, creating a more dense fog. The

dissipation of advection fog is similar to that of most fogs. If the relatively cooler surface becomes warmer, saturation levels would not be sufficient for fog. Also, synoptic patterns, such as fronts, pressure systems, and wind direction can act to remove advection fog (Stull, 1999).

1.2.2 Upslope Fog

Upslope fog forms as a result of adiabatic expansion and cooling of the air as it is orographically lifted up the side of a hilly surface (Kolb and Goodmanson, 1945). The fog forms when the cooling is sufficient enough to lower the air temperature to its dew point. As is the case with advection fog, upslope fog can form with moderate to strong winds and under cloudy skies (NWS, 2010). Under stable conditions, this ground-level cloud will form when the air parcel reaches its lifted-condensation-level. If condensation nuclei are added into the air mass from sources such as smoke or other continental particles, the fog will be denser and longer lasting. The most important factors affecting the formation of upslope fog are: lapse rate of the parcel, moisture levels at the surface and at the top of the hill, wind speed, and hill shape (Kolb and Goodmanson, 1945). Upslope fog will typically persist on the upslope side of the hill until the forcing at lower levels subsides, and/or there is a change in temperature or humidity levels.

1.2.3 Frontal Fog

Frontal fog, also known as precipitation fog, is usually divided into three types: warm front prefrontal fog, cold-front post-frontal fog, and frontal-passage fog (Byers, 1944). Prefrontal fog occurs in the cool stable air mass ahead of a warm front when warm stratiform precipitation falls on the cool side of the front. As the rain falls, it evaporates and

raises the dew point of the surrounding air (Gultepe, et al., 2008), making the nimbostratus cloud lower towards the surface. The northeastern U.S. is most at risk for this type of fog, due to mid-latitude cyclones occurring during the fall and winter producing the conditions necessary for prefrontal fog development. The mechanisms that form cold-front postfrontal fog are very similar to the aforementioned prefrontal fog, where evaporation from falling precipitation humidifies the air behind a cold front (Gultepe, et al., 2008). This type of fog is unlikely to be widespread due to the limited amount of precipitation that falls behind a cold front. However, stationary cold fronts could provide the ideal environment. Finally, frontal passage fog occurs when near-saturated air parcels from the warm and cold air masses mix together in calm wind environments (Gultepe, et al., 2008).

1.2.4 Radiation Fog

Radiation fog forms when radiative fluxes off the surface are sufficient to reduce the air temperature to its dew point (AMS, 1999). This fog type forms at night and typically requires clear skies and abundant low-level moisture. Clear skies are necessary in order for long-wave radiation to escape from the earth's surface, allowing temperatures to decrease rapidly. If dew point temperatures are sufficiently high enough, humidity levels can reach a critical point where fog will form. In addition, light winds typically below 2.5 m/s (Taylor, 1917), are also necessary for radiation fog to occur. If wind speeds are too strong, turbulence within the boundary layer would result, and low-level moist air would mix with drier air aloft. However, if winds are too calm, gravity will force the suspended water droplets to settle on the ground, creating dew/frost. Other favorable conditions for radiative fog formation include a small dew point depression at sunset, low-lying areas or

valleys, and large amounts of condensation nuclei.

Radiation fog forms upward from the ground as the night progresses and is usually deepest and most opaque around sunrise. Initially, the fog density decreases with height as temperatures at low-levels increase with height. However, as the fog continues to thicken at lower levels, it restricts the surface/ground from emitting long-wave radiation. When conditions reach this point, the maximum radiative cooling level moves upward toward the top of the fog layer. This results in denser fog at the top of the layer and initiates sinking cold thermals that act to turbulently mix the fog (Stull, 1999). Radiative cooling at the top of the fog can act to maintain and strengthen the fog intensity (Stull, 1999).

Radiation fog generally begins dissipating when the sun rises in the early morning hours, initiating mixing in the boundary layer. Through this method the surface warms quickly as it absorbs short-wave radiation and then warms the surrounding air. The water vapor droplets easily evaporate into the warmer air, resulting in dissipation of the fog. Radiation fog can also dissipate if there is a change in the overlying synoptic conditions, such as fronts or winds, or the dynamic forcing is altered. In the southern U.S., this type of fog is most problematic during the winter because the length of night is sufficiently long enough to drop the air temperature to the dew point. Interestingly, and as yet inexplicably, Tallahassee, Florida seems to be an exception to this, as it can experience more fog days during summer months.

The above classification of fog highlights some of the scenarios under which fog forms. However, it doesn't provide a clear depiction of the dynamics and physical processes involved due to its high temporal and spatial variability. Thus, the complex nature of fog is difficult to detect and forecast. Regardless, fog is still a boundary layer phenomenon so its

formation and influences can be better understood through climatic studies of surface conditions.

1.3 Previous Climatologies

There exists no comprehensive fog climatology for Florida, however a few studies touch on the climatology of fog in the region. Croft (1997) focused on the Southern U.S., specifically Alabama, Louisiana and Mississippi, and used local and regional climatic studies of fog combined with numerical models, soundings, satellite imagery and diagnostic software to forecast fog. The study found that in this region, the greatest average number of dense fog days occurs near the coastline and in the cool season, with the highest percentage of fog occurrence during the early morning hours. Forthun et al (2006) obtained Hourly Surface Airways datasets from 1948-2003 for 26 stations in the Southeastern U.S. and performed a linear regression on the dataset to examine annual and seasonal trends in the number of fog event days and fog duration. A variation of trends was reported in the southeast U.S., however decreasing trends were dominant. Six of these stations were located in Florida: Tallahassee, Jacksonville, Daytona Beach, Tampa, Palm Beach and Miami. The study found that four of the six Florida stations (DAB, JAX, MIA, TPA) showed significant decreasing/increasing trends in fog event days over the time period. Seasonally, TLH displayed no significant trends in any season. While they could not correlate the effect of land use, geography and population density to the trends in fog events, the study did show that the majority of fog days occurred in the winter, followed by autumn, spring and summer. These results line up with those done by Hardwick (1973) and Court and Gerston (1966), which indicate January as the peak fog month for most of

the southeast U.S.

Ray et al. (2014) conducted a study that comprehensively looks at the climatology of fog in Florida. As part of a limited FDOT contract, a five-year climatology of fog in Florida was undertaken. It used the only data available, the ASOS and AWOS stations with reliable visibility sensors. The locations of these are shown in Figure 1.1.

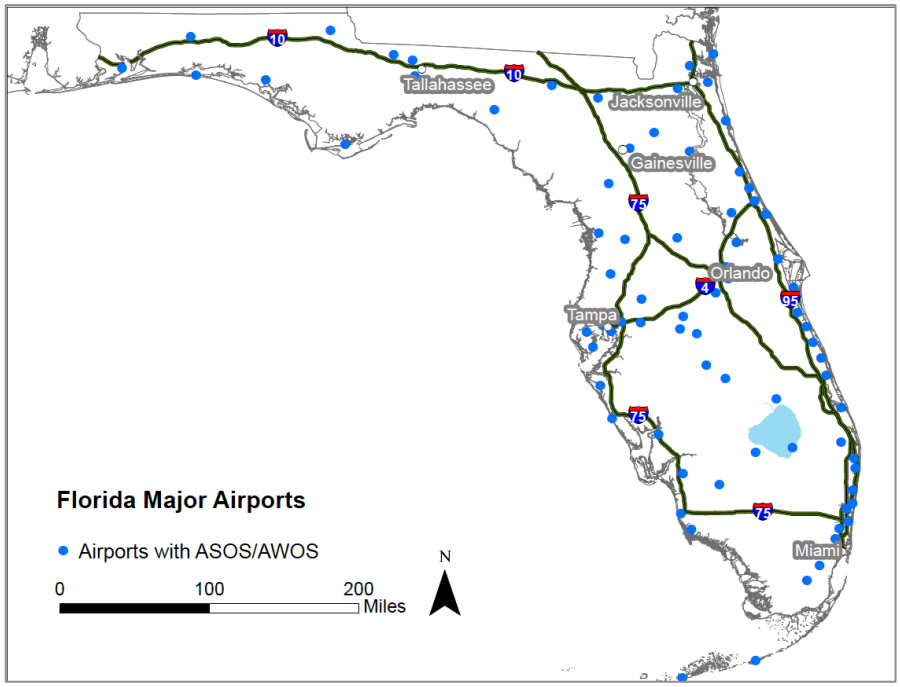

Figure 1.1: The location of Florida surface instruments.

The results from Ray's (2014) study are presented in Figure 1.2. While fog is highly variable spatially, it often tends to form in preferred locations. The ASOS/AWOS ground stations are not always sited to detect local fog in the area and certainly not its areal extent, however observations from these sites were used to develop a fog climatology for Florida.

His results show a greater prevalence of fog in the panhandle region of Florida as opposed to central and south Florida. The maximum at Tallahassee can be associated to two factors; one is the Tallahassee station being located at a relatively low elevation and

the other is due to a synoptic condition in the summer that favors fog formation in this region (Ray et al. 2014, Lavdas and Achtemeier 1995).

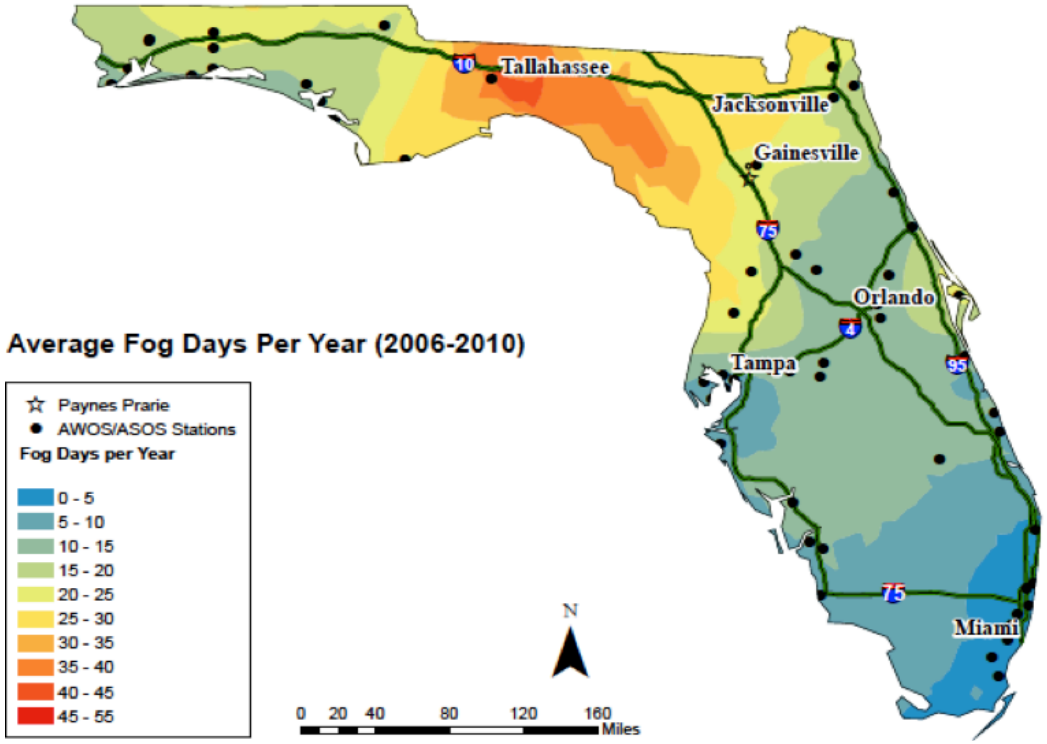

Figure 1.2 Average fog days per year from 2006-2010 based upon Ray et al. (2014). Station data was interpolated using kriging function.

1.4 Previous Work involving Satellite Fog Detection Techniques

Even though station observations provide ground-truth assessments of visibility and cloud cover for a point location, this form of data is discontinuous and can be sparse. Even if ground-based station data was available at a high spatial density, interpolating the data can be moot due to fog formation being a complex phenomenon influenced by multiple factors (Cermak et al, 2009). Thus, satellite data provides supplementary information on the horizontal coverage of fog.

Hunt (1973) theoretically determined two factors that lead to differences in the radiative properties of clouds in various visible and IR wavelengths of the spectrum. The first factor is due to fog droplets being less emissive in the 3.9-μm wavelength than in the 10.7-μm wavelength, whereas both emissivities are approximately the same for larger cloud droplets. This difference in emissivity between the long-wave and short wave IR channel is what causes a difference in temperature readings of a cloud observed by a satellite. The second factor was due to transmissivity differences allowing for more radiation from below the cloud top to be sensed in the SW IR channel. This explains why liquid low-level clouds appear colder in the SW IR channel than in the LW IR channel at night due to low transmissivity. Meanwhile, thin ice-phase cirrus clouds appear warmer in the SW IR channel due to higher transmissivity. Cloud free areas will usually have a small temperature difference between the SW and LW IR channels due to differential water vapor absorption (Findlater 1985). The above radiative properties of cloud were applied to remote sensing methods. These findings paved the way for satellite fog detection techniques where the difference in brightness temperatures between two wavelengths for a pixel is tested against a threshold value and classified as either low stratus (or fog)/clear/high cloud.

The first attempt at nighttime fog detection using multispectral IR images was in Great Britain by Eyre et al (1984). Advanced Very High Resolution Radiometer (AVHRR) imagery onboard a NOAA polar-orbiting satellite was used. This instrument produced imagery in three IR bands, one visible band and one near-IR band at a spatial resolution of 1.1-km. Temperature differences between channel 3 centered near 3.7-μm and channel 4 centered near 11.0-μm were used for fog detection. Temperature differences greater than

2.5 K signaled opaque clouds layer, temperature differences less than 0.5 K signaled an absence of clouds, and temperature differences between these two thresholds signaled either semitransparent fog or cloud. This methodology was soon after applied in the United States using AVHRR imagery (d'Entremont, 1986).

The nighttime dual channel fog detection technique was used on a wide arrange of platforms, including geostationary instruments. Lower resolution imagery from GOES-7 also proved to be capable of a nighttime bi-spectral fog detection technique (Ellrod et al., 1998). It had an onboard radiometer called the Visible and Infrared Spin Scan Radiometer (VISSR) Atmospheric Sounder (VAS), with the equivalent to the AVHRR channel 3 and 4 being channel 12 (3.9-μm) and channel 8 (11.2-μm), respectively. CH-8 was produced every 30 minutes and CH-12 was produced hourly. Even though CH-8 had a subpoint resolution of 6.9 km and CH-12 had a subpoint resolution of 13.8 km, both could still be used to derive an image detecting larger regions of fog or low clouds at night (Montgomery and Uccellini, 1985).

In April of 1994, GOES-8 was launched. It was the first satellite in the advanced GOES I-M series, which would provide imagery in the 3.9-μm and 10.7-μm IR windows (CH-2 and CH-4 respectively) at a subpoint resolution of 4.0 km (Menzel and Purdom, 1994). Not only was there a significant improvement in resolution in GOES-8, there was also an improvement in frequency of data scans. Separation of the imager and sounder instruments in GOES-8 allowed for imagery in both channels to be available at 15-30 minute intervals. Instrument noise was also reduced. Ellrod (1995) used the bispectral IR image differencing technique on both GOES-7 and GOES-8 IR imagery based on the emissive properties of fog shown in Figure 1.3. It was found to be efficient in detecting

fog/stratus over a wide variety of land and temperature regimes, as long as the fog wasn't obscured by overlying clouds (Underwood et al., 2004). Lower resolution GOES-7 imagery did demonstrate limitations in the detection of small and narrow areas of fog.

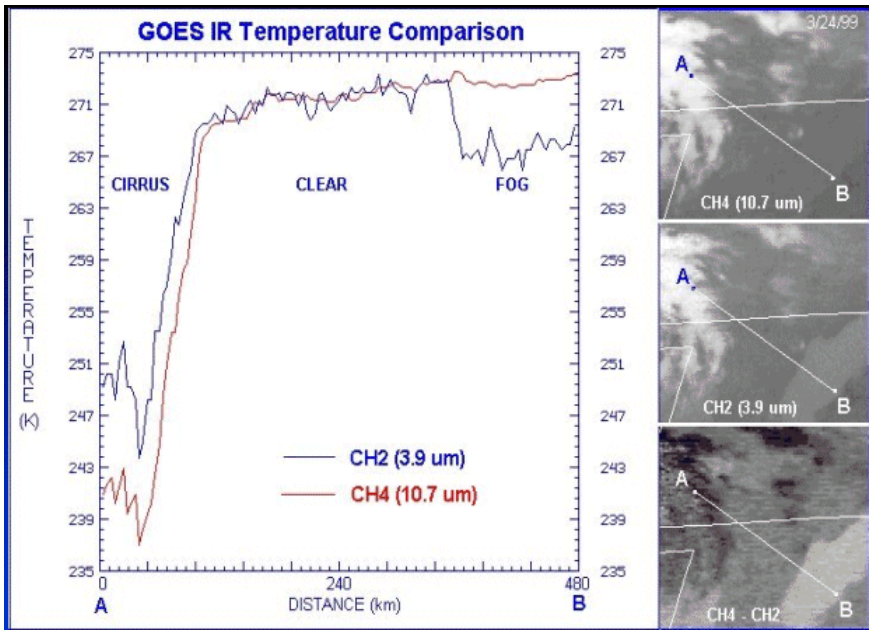

Figure 1.3: At nighttime, in fog regions, the difference between Ch4-Ch2 will be positive due to the emissivity difference of fog at 10.7-um and 3.9um. (Retrieved from Ellrod)

During daylight, sunlight reflected by liquid water clouds adds to the total observed radiance in the 3.9-μm wavelengths. The SW IR window's sensitivity to radiation causes the 3.9-μm temperatures to be larger than the 10.7-μm temperatures, so the liquid water clouds signal a negative temperature difference. Consequently, fog product becomes less useful during daytime hours. Fog and low clouds can be observed in the visible imagery at a high resolution of 1 km (Anderson et al, 1974). However, the use of the visible spectrum to detect fog during the daytime has its disadvantages. These include diurnal changes in illumination due to changes in solar elevation and difficulty in the distinction of fog from

other highly reflective surfaces, such as other types of clouds or snow. The scope of this study will focus on the nighttime fog detection scheme.

CHAPTER TWO

METHODOLOGY

2.1 Data Sources

Two sources of data are employed. The first is from Automated Surface Observing System (ASOS), and Automated Weather Observing System (AWOS) sites. The Federal Aviation Administration (FAA) operates and maintains AWOS units while the National Weather Service (NWS) largely operates ASOS units. The other source of data is from Geostationary Operational Environmental Satellite (GOES) system. The surface observations are used to validate the indications of fog that are derived from the satellite data. This study is a preliminary effort in understanding observed spatial variation in fog over the region of Florida using satellite imagery.

2.1.1 Surface Observations

ASOS and AWOS stations provide the standard atmospheric variables along with the Meteorological Terminal Aviation Routine Weather Report (METAR), which indicate the current weather conditions. ASOS measures air clarity, which is converted into a visibility value called the Sensor Equivalent Visibility (SEV) that is akin to what the human eye would see (Forthun et al. 2006). In terms of consistent visibility capabilities, ASOS/AWOS is proven to be more accurate than a station that reports based on human observations (NOAA, 1998). Typical reporting frequencies for AWOS units are every 20 minutes while ASOS units typically report at hourly intervals. While there are a few differences between ASOS and AWOS, they both are self-contained and designed to report observations without human involvement.

For the purposes of this study, horizontal visibility measurements along with the current weather condition reports from 71 ASOS/AWOS stations were used to determine whether fog was present. A fog event was identified as any time visibility below 5/8 of a statute mile (1 km) was reported. Although the indication for a dense fog advisory is a visibility of a quarter mile or less, 5/8 of a mile was used in order to obtain a large enough sample of fog events for the study. For the purpose of quality control, stations had to have data available for at least half the year in order to be included in the validation study. Station reports were excluded if they had missing visibility data. The data filtering resulted in a remaining 71 stations that were used in this study.

2.1.2 Satellite Observations

A year's worth of data before local dawn will be used to form a fog climatology of Florida. GOES-13 IR imagery from Geostationary Operational Environmental Satellite (GOES) is used due to its ability to capture images at a high frequency (every 30 minutes or less). It also has a spatial resolution of approximately 4-km at nadir for IR images and 1-km for visible images. Similar IR data at 1-km resolution is available from other instruments such as the AVHRR and MODIS but they run scans at low temporal scales (6-hourly at midlatitudes). Thus, they are typically used in adjunct to GOES data.

The National Oceanic and Atmospheric Administration (NOAA) manage the country's environmental satellite program. Within NOAA, the National Environmental Satellite, Data, and Information Service (NESDIS) office is responsible for the operation, processing, distribution and archiving of satellite data. The National Aeronautics and Space Administration (NASA) designs, develops and launches the satellite spacecraft. GOES along

with POES (Polar orbiting Operational Environmental Satellites) operations, provide a global satellite network (Davis, 2011). POES is in a sun-synchronous orbit 850-km above the earth and GOES is in a geo-synchronous orbit 35,890-km above the earth. Two separate spacecraft, GOES-East (located at 75°W) and GOES-West (located at 135°W), provide coverage of the western hemisphere. Together they observe southern Canada, the contiguous U.S., the eastern Pacific Ocean, the western Atlantic Ocean basins, Central America and South America. While POES provides data depicting daily global coverage used for monitoring long-term climate and atmospheric trends, GOES is capable of observing events and tracking their evolution in real-time (Davis, 2011).

2.2 Geostationary Operational Environmental Satellite (GOES)

The Geostationary Operational Environmental Satellite program began in May 1974 with its prototype, the Synchronous Meteorological Satellite-1 (SMS-1) and later in October 1975 launched GOES-1. Both satellites featured the visible/IR Spin Scan Radiometer (VISSR) onboard, which allowed for observations of cloud and surface temperatures, cloud heights and wind fields. Advancements were made by the launch of GOES-4 in 1980; the operational GOES system had been implemented and the instrument onboard was capable of profiling vertical temperature and water vapor. In the 1980s, development for the GOES I-M were made which entailed a three-axis body stabilized geostationary environmental satellite with the first fully independent sounder and an updated imager (Davis, 2011). It launched in April 1994 as GOES-9 and was capable of observing the Earth in 24 different spectral channels and wavelengths between 0.6-14.7-μm (Weinreb et al., 1997).

Since 1974, there have been sixteen GOES launches. GOES -12/-13/-14/-15 are the satellites available currently for operational use. GOES-12 is designated GOES-South and is located at 60˚W. GOES-15 was launched in March 2010 and designated as GOES-West, GOES-13 was launched in May 2006 and designated GOES-East, and GOES-14 is currently in storage at 90˚W. GOES-13 experienced an outage due to an anomaly from 23 September 2012 to 18 October 2012. GOES-14 was placed into service during the GOES-13 outage (NOAA 2012). Therefore, this study utilizes data from both GOES-13 and GOES-14.

2.2.1 GOES Data Acquisition

The GOES spacecraft performs three main functions: environmental sensing, data collection and data broadcast. The environmental sensing entails the acquisition, processing and dissemination of the imaging and sounding data along with independent monitoring of the space environment. The five-channel imager and the nineteen-channel sounder perform the remote sensing. The raw imager and sounder output data is transmitted in real-time to the Command and Data Acquisition Station (CDA) located in Wallops Island, Virginia. The CDA processes, calibrates and geo-locates the data before converting it to GOES Variable Data (GVAR) format (Weinreb et al., 1997). The GVAR data is retransmitted to the satellite, which then broadcasts it to independent users in the data stream. The above sensing, data processing, and final distribution of data is all done in real-time in order to meet NOAA spacecraft command schedules and requirements. There are currently three operational imaging modes designated as Routine, Rapid Scan and Super Rapid Scan. The routine schedule provides an image every 15 minutes. Further information

on the GOES-East Imager Routine regarding coverage, scan duration and scan time is given in Table C2 of Appendix C.

The imager onboard the spacecraft senses radiant and solar-reflected energy from sampled areas of the earth. The imager makes observations in five different spectral channels by scanning in an east-west direction along an 8-km (north-south) wide path using a two-axis mirror scan system. Stationary filters and beam splitters work to separate the one visible channel and four IR channels. The GOES pixels are square, but are oversampled along the scan-line (in the east-west direction), so they have twice the spatial sampling in this direction as compared to the north-south direction (Menzel and Purdom, 1994). This is why the GOES GVAR projection appears stretched in the east-west direction when displayed. Table C1 of Appendix C gives information about the current GOES imager channels, including approximate spectral widths, central wavelength, and approximate sub-satellite point resolutions. In this study, IR channel 2 (3.9-μm) and channel 4 (10.7-μm) are employed.

GOES data is available in real-time, but past data is archived and distributed by the NOAA National Climatic Data Center (NCDC). Data is available in a selection of file formats that can be requested and transferred to your operating system. 'Area' format files are specific to GOES images and store the data in GVAR format along with its calibration and navigational information. NOAA has a Weather Toolkit available online which can be downloaded to one's desktop and used for the conversion from Area format to either binary, ASCII, netCDF, or geoTIFF files. However, this would require converting 10-bit data to 8-bit data, which results in a loss of precision in the temperature values necessary in the

fog product. Thus, fog images generated from the highest bit depth data (GVAR counts) are preferred (Hillger, 1999). The Man Computer Interactive Data Access System (McIdas) is a software program unique to the processing and displaying of Area files along with other forms of meteorological data. True to its name, McIdas provides a simpler way for 'man' to handle the untamed form of this data, and retrieve the desired information through 'computer interaction' (Lazzara et al. 1999).

The raw data received from the satellite is rendered useless unless calibrated or transformed into meaningful physical units (such as radiance or temperature) and navigated relative to time and space. Therefore, the raw image data received from the satellite is processed at the CDA station and is converted into scaled radiances packaged into 10-bit GVAR words. The GVAR data, along with ancillary data, is stored in an Area file consisting of various blocks of information. These include: the directory block which catalogs information specific to the image object, the auxiliary block containing any information created by the user, the navigation block comprising of the earth coordinates associated with each image pixel, the calibration block containing the data needed to convert between raw image sensor data to physical units (albedo, temperature or visible brightness) and the data block containing the matrix of image data values (Weinreb et al., 1997). McIdas handles the processing of the data blocks, allowing for much easier analysis, manipulation and display of the imager data.

Users can derive scene radiances from the 10-bit GVAR counts stored in the IR image data block (Weinreb et al., 1997). This process is described in Appendix D in further detail. There are three intermediate steps involved in the conversion between GOES

infrared 10-bit GVAR counts, radiances, temperatures, and 8-bit brightness counts (temperatures). McIdas software performs these conversions automatically when reading in an area file. The user can specify which unit will be used for display or calculations. For the purposes of deriving a fog product, IR temperature values will be used.

2.2.2 Co-registration Error Correction

In the process of examining the fog product over Florida, evidence of a GOES-13 CH-4 – CH-2 collocation issue was discerned. Nearly all of the difference images displayed a whiter edge along the western coast of Florida and a darker edge along the eastern coast. This type of artifact was also seen in locations where stations did not report fog or low cloud conditions, however the satellite detected fog in the same location. These false positives were indicative of a misalignment between the GOES IR channels, causing an error in bi-spectral measurements. The errors were seemingly smal, but significant when the retrieval algorithm depends on the difference between two channels. Work done by the Cooperative Institute for Meteorological Satellite Studies (CIMMS), as well as Grotenhuis et al (2012) discovered that the co-registration error between channels 4 and 2 is of sub-pixel resolution but can range anywhere from 0.5-1.5 in the east/west direction. Efforts have been made to accomplish GOES Imager co-registration. The most recent and effective is an area-based approach that incorporates a Fast Fourier Transformation Resampling (FFTR) algorithm developed by Li et al (2014). It relies on maximizing the cross correlation of the Fourier Transforms of the spectra for each scan and then averaging the correction. This method, which determines the offset and resamples the data, is detailed in Appendix D.

Because the co-registration errors for GOES-13 are at the sub-pixel level, image resampling needs to be done to one of the channels. CH-2 images were resampled using the FFTR algorithm because the CH-4 (10.7-μm) images were more aligned with its visible images, suggesting that the navigation on channel 4 is more correct. The resampled CH-2 and original CH-4 images are used for deriving the fog product.

2.2.3 GOES Fog Retrieval

The visible channel measures the albedo coming from the earth in the visible portion of the spectrum. Thus, its utility is largely restricted to daytime viewing. The IR portion of the spectrum measures the radiance of the earth's emitted radiation. Different channels measure different portions of the Plank's curve appropriate to the earth's temperature at the point being viewed. However, different gases or clouds can attenuate that signal and the effect will vary with the wavelength of the emitted radiation that a particular channel perceives.

By comparing two IR channels (CH-2 and CH-4), it is possible to detect the presence of wide spread fog at night. This is because CH-2 is much more sensitive to temperature and fog reduces the received radiance more than it is attenuated by CH-4. Thus the temperature difference quantity (CH-4 – CH-2) can be used as a fog product to identify regions where fog might be present at night.

For ease of analysis, the sample consists of one scan time per day for a period of one year (2012). Using CH-4 - CH-2 images from fully dark times is preferable. One reason is because fog formation is maximum between midnight and sunrise and tends to be thickest right before daybreak due to the cumulative radiative cooling effects of the atmosphere and the surface (Findlater, 1985). Another reason is because CH-2 is highly impacted by

reflected sunlight, so 3.9-μm imagery with encroaching sunlight will show distinctly warmer temperature values. At a minimum, it is best to limit CH-4 – CH-2 imagery to those pixels where the solar zenith angle (SZA) indicates no solar influence. To be conservative, a SZA greater than 90 degrees was used. The greatest variation over daybreak in Florida is in the east-west direction. There is approximately a 7-8 degree difference in longitude between the east coast of Florida and its western border. This corresponds to about a difference in 30 minutes in the time of daybreak from the eastern end to the western end. Since all orders of data are done in UTC (Universal Time Coordinates), the conversion between UTC, local time and daylight savings time is: EST= UTC -5 hours or EDT=UTC-4 hours.

Tallahassee, Florida is located at coordinates 30.4°N, 84.35°W. It is roughly equidistant from the eastern and western borders of the state; therefore it is used as a reference for determining what satellite pass times to use. The time of daybreak (UTC) in Tallahassee, FL is given in Table 2.1 in units of hours: minutes.

Jan	**Feb**	**Mar**	**Apr**	**May**	**Jun**	**Jul**	**Aug**	**Sep**	**Oct**	**Nov**	**Dec**
12:34	12:28	12:03	11:25	10:53	10:35	10:39	10:55	11:14	11:31	11:52	12:17

Table 2.1: Time in UTC for daybreak on the first of the indicated month in Tallahassee, Florida.

A plot of sunrise times for Tallahassee is shown in Figure 2.1 where the times are in fractional hours UTC. The asymmetry is due to the earth's elliptical orbit around the sun and because the time between equinoxes is not equal for the summer and winter seasons. The fitted cosine model is:

$$daybreak\ time\ (UTC) = 11.57 - \cos\left[\frac{2\pi}{12}(m - 6.7)\right]$$

where m is the number of the month (1-12). The average sunrise time (UTC) is 11.57 hours and the daybreak difference over the year is approximately two hours. After an extensive examination of 3.9-μm imagery well before to well after sunrise, it was concluded that on any given day, 3.9-μm imagery at least 30 minutes prior to daybreak in Tallahassee is not affected by sunlight. The GOES-East Imager Northern Hemisphere scan sector is available every half hour on the routine schedule, so the scan time chosen for each day is 25-75 minutes prior to daybreak in Tallahassee.

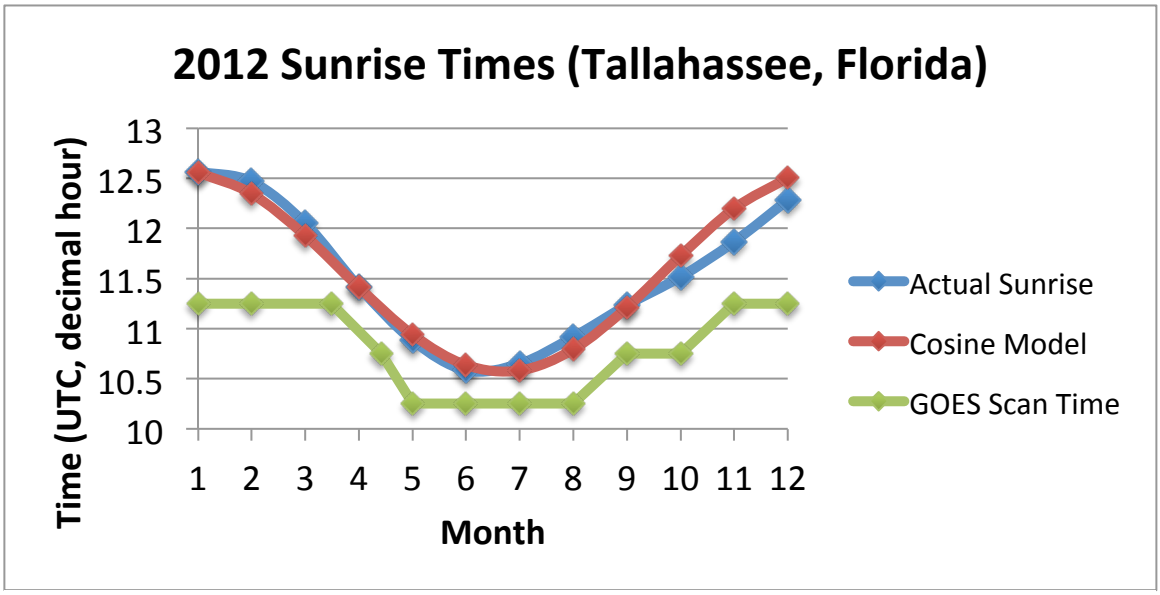

Figure 2.1: Plot of actual sunrise times for the year (month indicated numerically) for Tallahassee, Florida. The green line is the GOES scan time images used for 2012. Times are in fractional hours UTC.

The fog image results must be compared to the surface observations to both assess their accuracy, design an optimum filter and to know how to best scale the satellite observations to extract the best information that can be obtained from the fog. Threshold values of observed brightness temperature differences are determined dynamically. This

threshold depends on many factors including geography, season and regional stratification of the data. Threshold values used for detecting fog in the western U.S. may not be accurate for detecting fog in the southeastern U.S. (Cermak and Bendix, 2008). Evidence of this is seen in coastal regions where fog is present but BTDs smaller than the threshold value is observed due to the larger droplet sizes found in marine stratus (Lee et al. 1997). This can be corrected by designating a lower threshold value for fog detection, while taking into account that this may increase false positives over land (Ellrod 2002).

Threshold decisions were determined by creating a series of histograms of brightness temperature differences. First, a histogram with all of the temperature differences was analyzed. Within this BTD frequency distribution, a clear-sky peak within a certain range of values is identified. The nearest relative minimum located closest to the negative BTD values is also identified. This minimum value is used as the threshold to distinguish between a cloudy vs. clear pixel.

Another threshold is needed to discriminate between fog and non-fog pixels. The station pixel values were extracted from the fog product images and divided into two separate tables based on whether the co-located observation reported fog or no fog that morning. Within each table the brightness temperature difference (in 8-bit counts) was separated into 256 bins ranging from 0-255 with a bin size of 1 count. One brightness count is equivalent to a BTD of 0.1 K. Total occurrences of fog and no fog events for each bin were used to estimate the probability that fog is present given a pixel's bi-spectral value. Verification of the fog product was then done using a series of contingency tests on varying threshold values. This approach involves a binary comparison between a classification

scheme and a reference. In this case, the ASOS/AWOS observations were used as the "ground truth" to verify the fog product results.

The joint probability of presence or absence of fog is assessed between the observations and the forecast (satellite signal) for a given time and location and compared using the contingency matrix described below:

		Station Observation	
Satellite Detection		Yes	No
	Yes	A (hit)	B (false alarm)
	No	C (miss)	D (correct negative)
	Cirrus	E (removed from validation)	F (removed from validation)

Table 2.2: Contingency Table used for validating the fog product.

$$POD = \frac{A}{A + C}$$

$$FAR = \frac{B}{A + B}$$

$$PFD = \frac{B}{B + D}$$

$$PC = \frac{A + D}{A + B + C + D}$$

$$BS = \frac{A + C}{A + B}$$

$$CSI = \frac{A}{A + B + C}$$

$$HK = \frac{(AD - BC)}{(A + C)(B + D)} = POD - PFD$$

A, B, C and D are used to calculate a series of skill scores. The total number of non-events is $N_0=B+D$, the total number of events is $N_1=A+C$, and the total sample size is $N=N_0+N_1$. Even though this is a 2x2 matrix, there are only two degrees of freedom given the constraints of N_0 and N_1 (Marzban, 1998). The statistical indicators calculated are probability of detection (POD), false alarm rate (FAR), probability of false detection (PFD), percent correct (PC), bias score (BS), critical success index (CSI) and the Hanssen-Kuiper skill score (HK):

POD gives the fraction of correctly detected observations with a POD=1 indicating best detection. FAR calculates the fraction of false alarms with a FAR=0 indicating best performance. The PFD calculates the rate at which non-fog events are misclassified as fog. A PFD of 1 shows situations where only misclassifications occurred. The PC is the ratio of correctly detected events (both fog and non-fog events) out of the total number of events. The BS provides information on whether the satellite overestimates (BS<1) or underestimates (BS>1) fog frequency. The CSI provides a measure of overall classification accuracy where higher values indicate higher skill. The POD and PFD are expressed relative to one another in the HK score. It ranges from -1 to 1 (with 0 indicating no skill) and characterizes how well the product discriminates between fog events and non-fog events.

This combination of verification methods and appropriate observations are used to determine which values of BTD perform best in detecting fog by introducing a decision threshold. If the skill measurement appears to be inequitable, than the decision threshold is lowered or raised in order to optimize the score. A program was written to optimize the highest success rate of detecting fog between threshold values of brightness temperature differences using the ASOS/AWOS reports as reference.

The fog product itself involves the simple sequential application of these thresholds to classify each pixel as either fog, clear (no fog) or high cloud. All 366 fog images were processed and an output mask was created for each image based on the classification scheme. The results were averaged for each pixel to obtain information on the spatial characteristic of fog detected from the satellite. The aggregated fog product results were mapped onto a grid with 5x5-km pixel resolution. The stations' bias errors were interpolated over the state of Florida and were used to adjust the satellite-derived fog frequencies. This was accomplished using ArcGIS and both kriging and inverse distance weighting interpolation techniques based on the observed data. Both interpolation methods were used to assess which produced the most realistic surface. A classified map of fog frequency was prepared with nine separate classes at equal intervals. Comparison of fog events was made to seasonal patterns of fog frequency as well as the annual pattern of fog frequency.

As stated earlier, the fog detection scheme is limited by its spatial resolution, as well as the inability to examine how thick the fog is from above. It is important to realize that the satellite information is *not* more accurate than the ground observation in determining if fog exists.

2.2.4 GOES Fog Product Image

The brightness of the fog image is displayed on an 8-bit scale with values ranging from 0-255. In a given fog image, the low clouds appear as white, the ground appears as gray, high clouds are black and high multi-layered or thunderstorm cloud tops have a salt and pepper appearance. This is due due to the imager's sensitivity to extremely cold temperatures (below -40 degrees). Color enhancements are typically applied to the

fog/low cloud images with appearing yellow and cirrus clouds appearing blue. An example of an enhanced fog product image is shown below in Figure 2.2. The fog/low cloud appears in the images when the low cloud is wider than 2 miles, and has a thickness of approximately 100 feet. Therefore, the fog product is likely to distinguish widespread low stratus and fog conditions but not thin and local fog and haze cases.

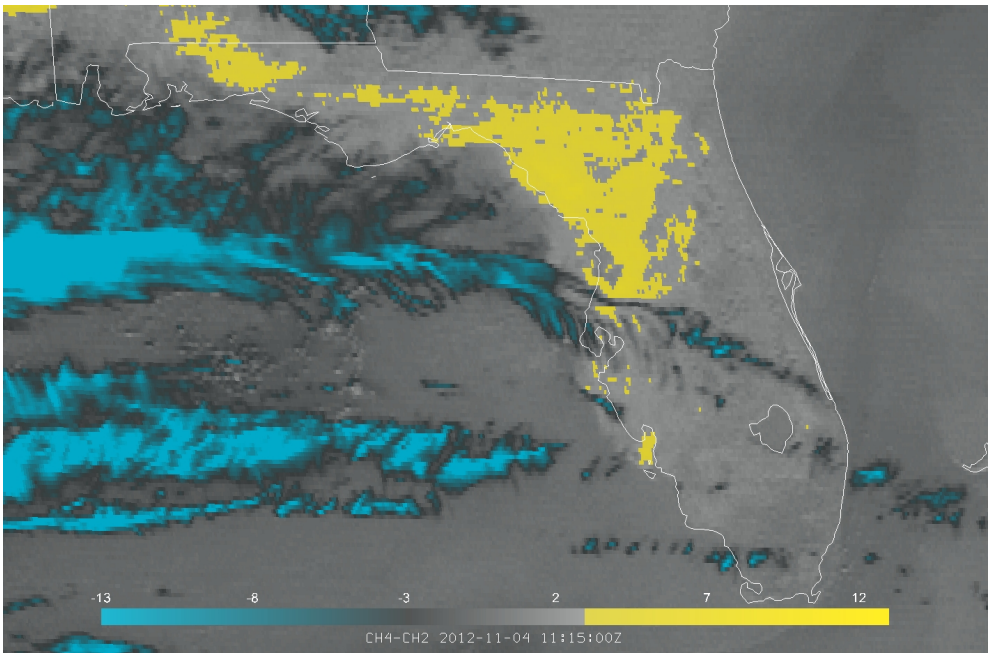

Figure 2.2: Enhanced GOES Fog/Low Cloud Product for November 04, 2012 at 11:15 UTC.

CHAPTER THREE

RESULTS

3.1 ASOS/AWOS Climatology

A fog frequency map was first constructed based on point observations for the year 2012, the year that is the focus of this research. A fog day was identified if the ASOS/AWOS station reported fog conditions as well as a visibility of less than 5/8 statute miles between the hours of 9 UTC and 12 UTC. These station totals were then interpolated over the state of Florida using a kriging interpolation method in ArcGIS. Kriging is a stochastic interpolation technique that utilizes semi-variogram models to fit a surface across irregularly spaced data points (Ward and Croft, 2008). The results are presented in Figure 3.1. The general patterns shown agree fairly well with those seen in the longer time series in Figure 1.2. Similar to the five-year fog day averages, a decreasing trend in fog occurrence from north to south is evident in 2012. While fog was still most prevalent in north Florida, the maximum fog occurrences were in the western panhandle as opposed to Tallahassee. Also, the frequency of fog in central Florida was greater in 2012 than the 2006-2010 average.

The distribution of number of stations with fog per day exhibits the expected maximum during the cold weather months. Although the data shows large day-to-day variation, the 30-day running average does exhibit a sinusoidal dependency. This is presented in Figure 3.2.

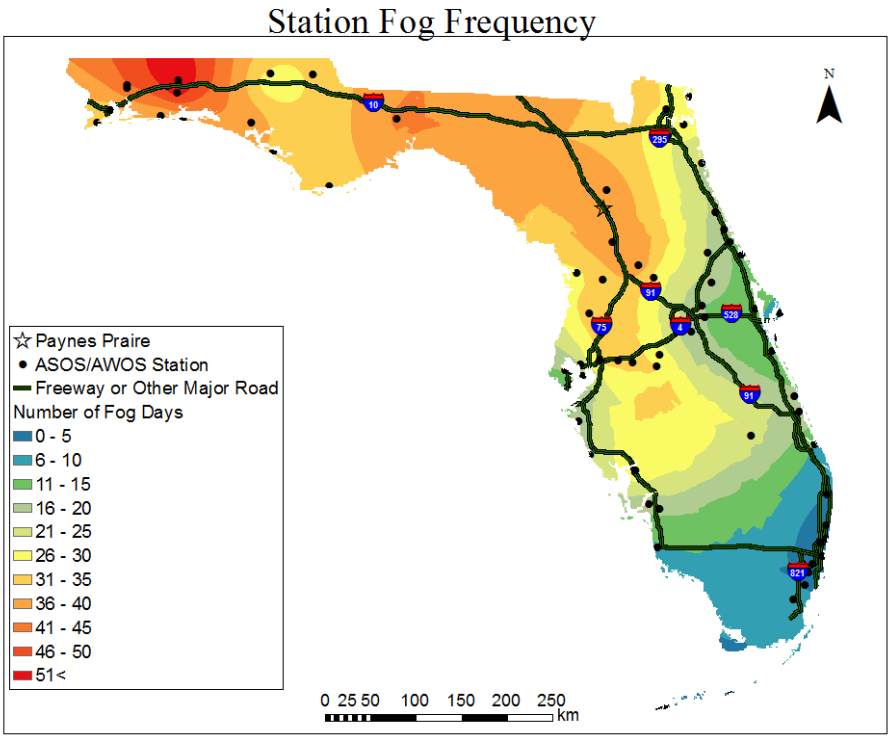

Figure 3.1: Fog days for the year 2012 from the ASOS/AWOS stations. This can be compared to the more extensive dataset given in Figs. 1.2.

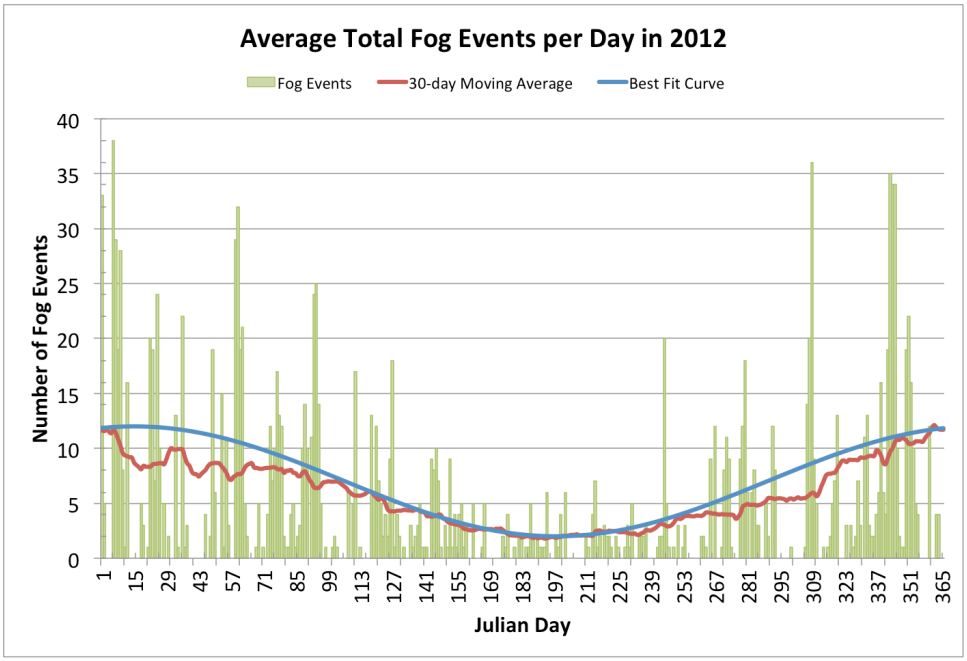

Figure 3.2: Light green indicates the number (out of 71 possible stations) that experienced fog on a given day. The red line is a 30-day running average and the blue curve a cosine fit to the data.

The formula for the cosine curve is

$$\boldsymbol{number\ of\ fog\ events = 7cos\left[\frac{2\pi(JD-15)}{366}\right] + 2} \qquad \textbf{(3.1)}$$

where JD is the Julian Day. The standard deviation of the fit of the cosine wave is approximately 8 stations. This is evidenced by the large day-to-day variations in the cooler months. The overall number of fog events for 2012 reported by the 71 AWOS/ASOS sites was 6.3%, with 1,586 fog events reported out of the 25,365 station observations.

3.2 GOES Satellite Data

The earth reflects and emits radiation over a wide spectrum of frequencies. The reflectance is centered in the visual part of the spectrum while the emittance is in the infrared part of the frequency domain. The GOES Imager data is collected in a number of channels, each of which incorporates either reflectance or radiance, which is filtered in a number of frequency domains. This study utilizes two IR channels: 2 and 4. The fog product is obtained by subtracting CH-2 from CH-4 brightness temperatures and producing a binary mask indicating whether fog is present or absent based on BTD values.

The fog product is extremely sensitive to any artifacts or instrument noise within the imagery because it utilizes bispectral tests. Calculating the CH4-CH2 co-registration error for each image and resampling the CH2 image by this error removed instrument noise. The co-registration error varies from day-to-day and time-to-time. The correction is given in Appendix E.

3.3 Fog

The ASOS/AWOS observations were compared with the collocated satellite pixel values. The frequency distribution of non-fog events versus fog-events and their respective bispectral pixel difference values were compared. Figure 3.3 shows the brightness count values for the 1,586 fog events versus the 23,779 non-fog events. Doswell et al. (1990) considers this preferred proportion of non-fog events to fog events to be characteristic of a rare-event situation. Based on these distributions it can be assumed that for any given brightness difference value, the likelihood of a non-fog event over a fog event will always be greater.

Figure 3.4 shows the BTD distribution of fog vs. non-fog events on a similar scale. The fog events peak at 166 and 169, which is equivalent to a CH4-CH2 TD of 1.6 and 1.9 K, respectively. The non-fog events cluster around 158 brightness counts, which is equivalent to a TD of 0.8 K. The peaks in these distributions provide some insight into what optimal threshold will discriminate between clear and fog pixels.

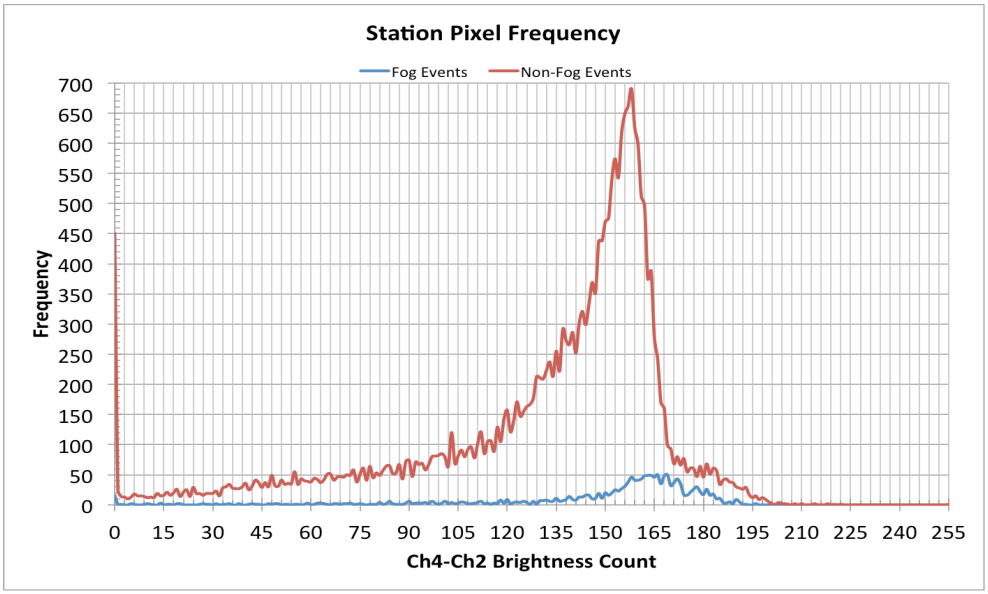

Figure 3.3: Distribution of pixel brightness values for both fog (blue line) and non-fog (red line) events.

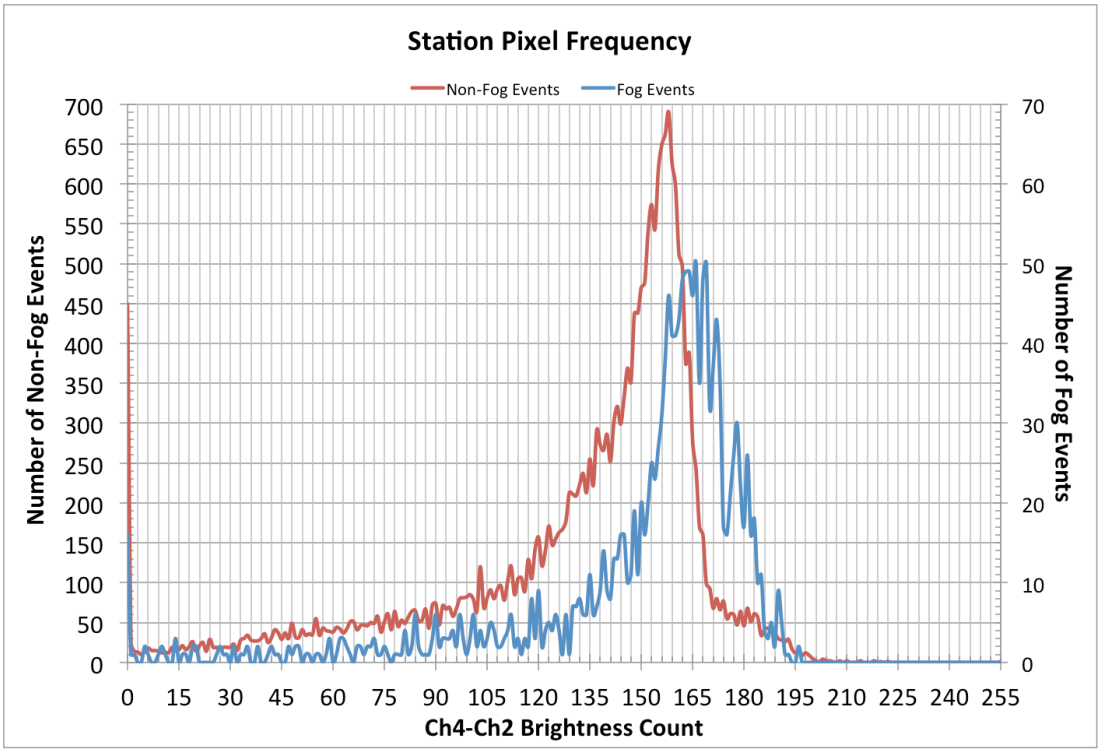

Figure 3.4: Distribution of pixel brightness values for both fog and non-fog events on proportional scale

The fog product itself involves a simple sequential application of thresholds used to classify a pixel as either fog, clear (no fog) or high cloud. At night, IR temperature differences for high cirrus clouds tend to be large and negative. In this study, temperature differences less than -3 K (0-120 brightness counts) are flagged as cirrus/high clouds. The threshold value for cirrus clouds was chosen based on past studies and by manual inspection of images in the dataset (Ellrod 1995, Cermak 2005, Cermak 2012).

The next step was determining the threshold value to discriminate between fog and non-fog pixels. Contingency tables (described in the previous chapter) were used to calculate the performance of the fog product for each possible threshold value based on ASOS/AWOS observations. Fog thresholds for brightness count differences greater than 120 are considered. Pixel values between the high cloud and fog threshold ($120<BTD<T_F$)

were flagged as non-fog (0 in the output mask) and values above the fog threshold ($BTD \geq T_f$) were flagged as fog (1 in the output mask).

Overlying clouds in images do not allow for proper detection of fog/low cloud events, causing errors in the statistical indicators computed. Therefore, these high or multi-layer cloud situations are accounted for and removed from the fog product validation altogether (Cermak and Bendix, 2007). Eliminating the 6,240 overlying cloud situations from validation resulted in a sample of 19,125 observations as opposed to the original 25,365 station observations. Figure 3.5 shows the POD, FAR, PFD, BS, CSI and HK for detecting fog above all the possible threshold values ($\geq T_f$) between 150 and 190. The CSI is maximum at 166, HK is maximum at approximately 161 and the BS is 1 between 173-174. Figure 3.6 shows the POD and CSI for detecting fog at each individual threshold value ($=T_f$), with the frequency of fog events at each pixel value also plotted. This provides a notion of how successful each distinct brightness count value is in detecting fog based on the 2012 station observations. The max CSI is found at the BTD value of 169. The distributions in these figures insinuate that there is a range of threshold values that best represents fog in the bispectral images. The optimal threshold window was determined by implementing a contingency table to examine various threshold window widths and find where the maximum value of CSI existed. These results are shown in Figure 3.7.

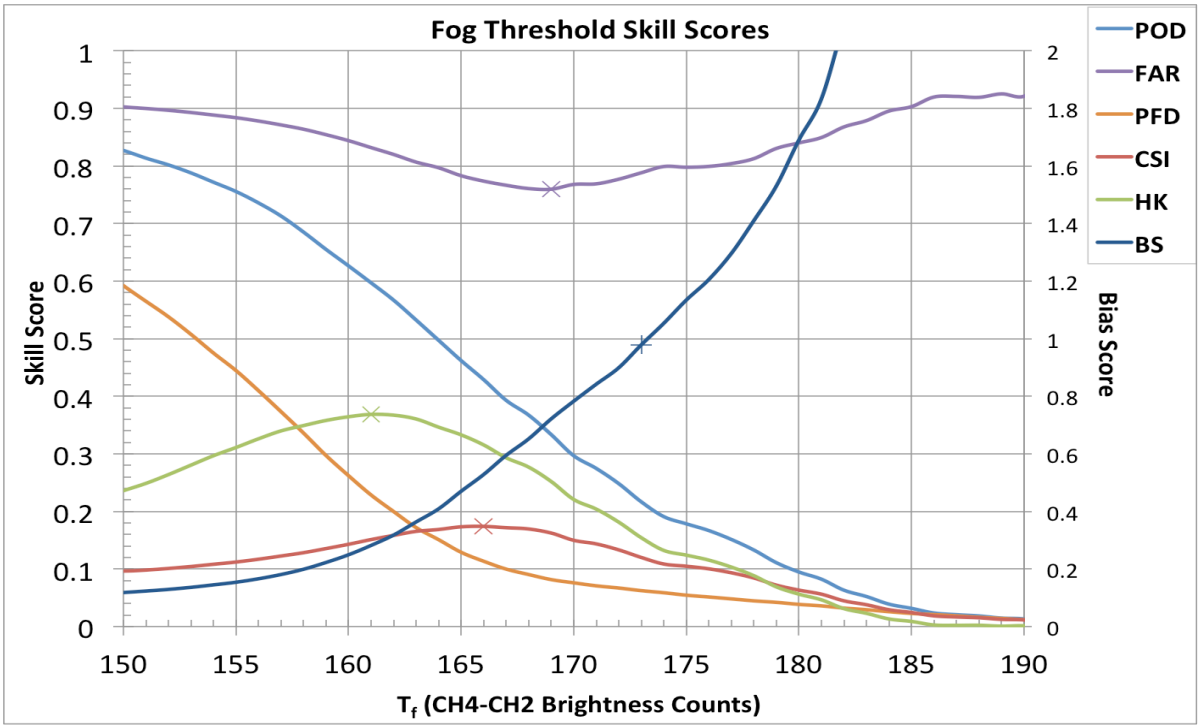

Figure 3.5: Skill scores for detecting fog above values of T_f

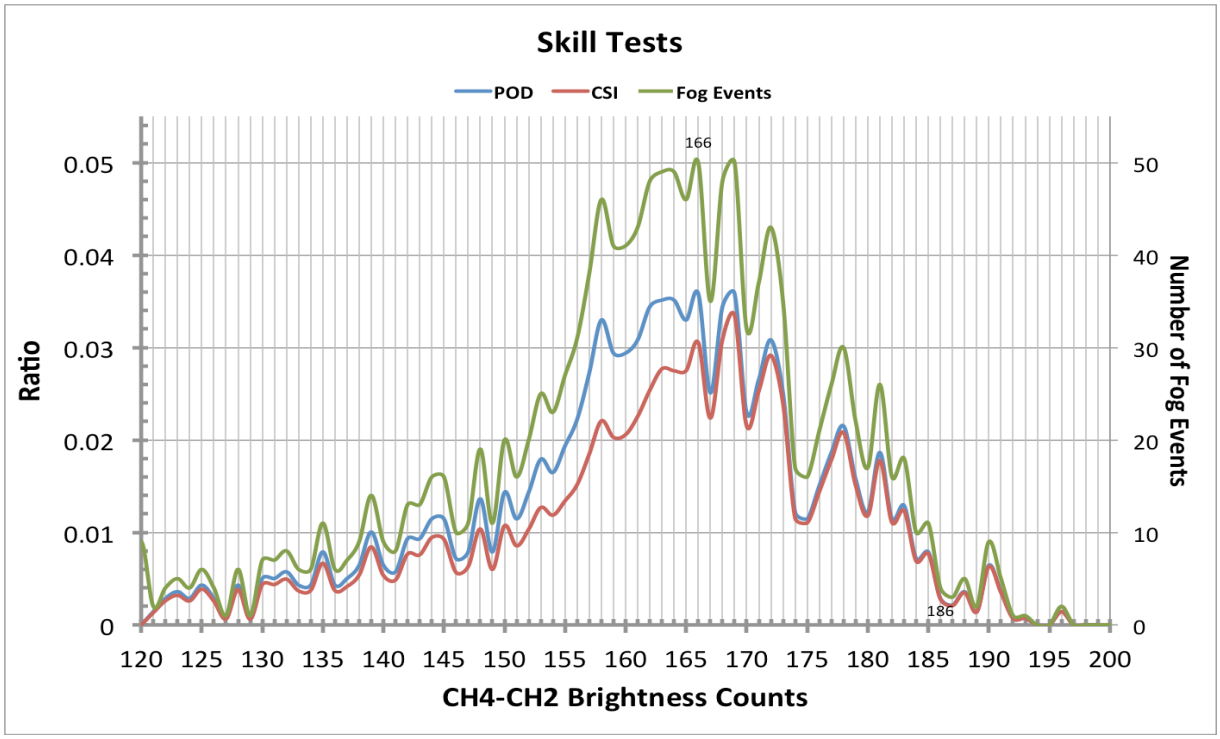

Figure 3.6: POD, CSI and number of fog events for each individual brightness count value. POD (blue) and CSI (red) are plotted on the left axis and number of fog events (green) is plotted on the right axis.

Figure 3.7: CSI values for set of window locations and widths. The ideal threshold range were determined to be for a window of 20 brightness values wide and centered at a brightness difference value of 176. This is based on the analysis of 25,365 satellite observations vs. ASOS/AWOS ground truth data.

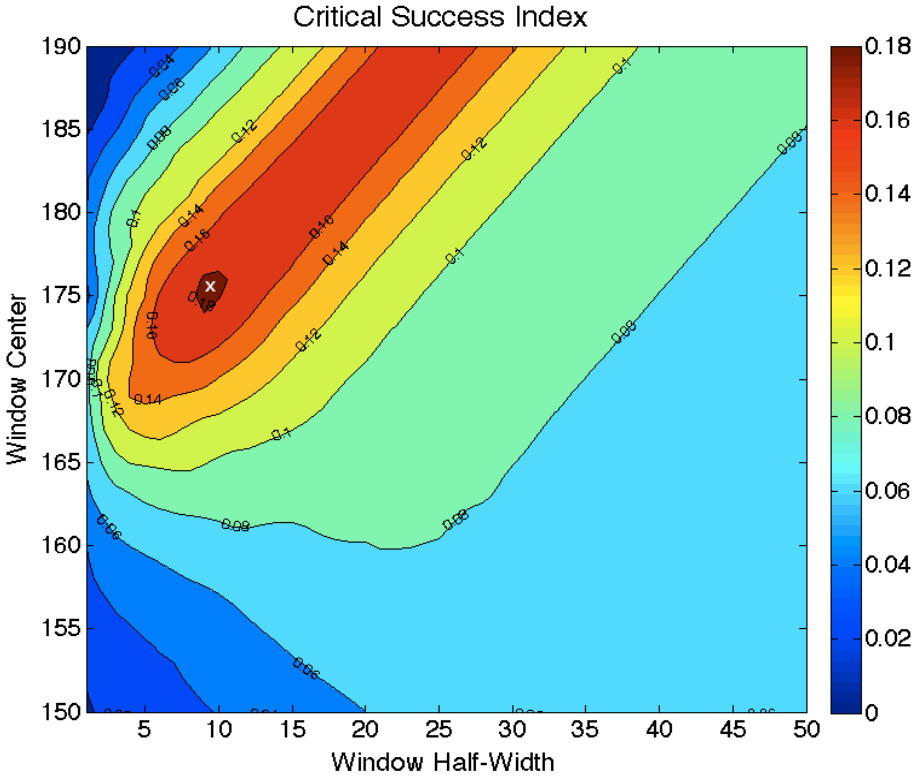

The maximum CSI value is found at a threshold centered around 176 brightness counts and 20 brightness counts wide. Therefore, brightness values of 166-186 are chosen as the threshold values for detecting fog in the pixel classification scheme. These BTD values correspond to temperature differences of 1.6-3.6 K. This result agrees with the scores calculated in Figures 3.5 and 3.6. The contingency matrix for the chosen fog threshold of 166-186 BTD is shown below in Table 3.1.

		Station Observation		
Satellite Detection		Yes	No	Totals
	Yes	556	1,670	2,226
	No	815	16,084	16,899
	Cirrus	215 (removed from validation)	6,025 (removed from validation)	6,240
	Totals	1,586	23,779	25,365

Table 3.1: Contingency table results.

Using the chosen threshold window results in a CSI of 18%, a POD of 41%, PFD of 9% and an HK of 32%. This means that while false detections are generally low, a good portion of the fog situations go undetected by the satellite. This is explained by the data comparison approach; the classification applied to the METAR data identifies fog based on ground level visibilities (Cermak and Bendix, 2007). The visibility measurement at the station is a point measurement and may not be representative of what is seen in the corresponding satellite pixel. While an effort was made to remove cirrus cloud cases from the contingency table, some multi-layered cloud cases may have still been included. This would negatively impact the validation skill scores. Schaefer, (1990) also demonstrated that the CSI tends to be biased towards samples where the frequency of an event is greater. Therefore, the CSI may be a misleading indicator of skill when assessing the fog product across different regimes. The bias score of 0.62 indicates that the fog product generally over-detects fog events across the state.

Computing the frequencies for each individual station showed variation in skill scores amongst the stations. The average number of fog days per station for 2012 is 22

with a standard deviation of 16.5. GNV, JAX, TPA and NSE obtained the highest CSIs of 0.30 and greater. The highest HK score was from TPA, TIX, and MCO with 0.81, 0.63 and 0.63 respectively. CEW was the station with the maximum fog days and also was the least biased, with a bias score of 1.09.

Note that given the nature of fog, these scores are rather low. Also these scores are scalar and due to the rarity of fog events, optimizing any of the validation statistics will induce some form of bias (Marzban, 1998). Figures 3.8 and 3.9 illustrate how the fog product performed across the state based on ASOS/AWOS observations. The scores were calculated for each station and then interpolated using kriging. The CSI and POD both have similar spatial patterns. The best performance in detection of fog is seen in the northeast portion of the state.

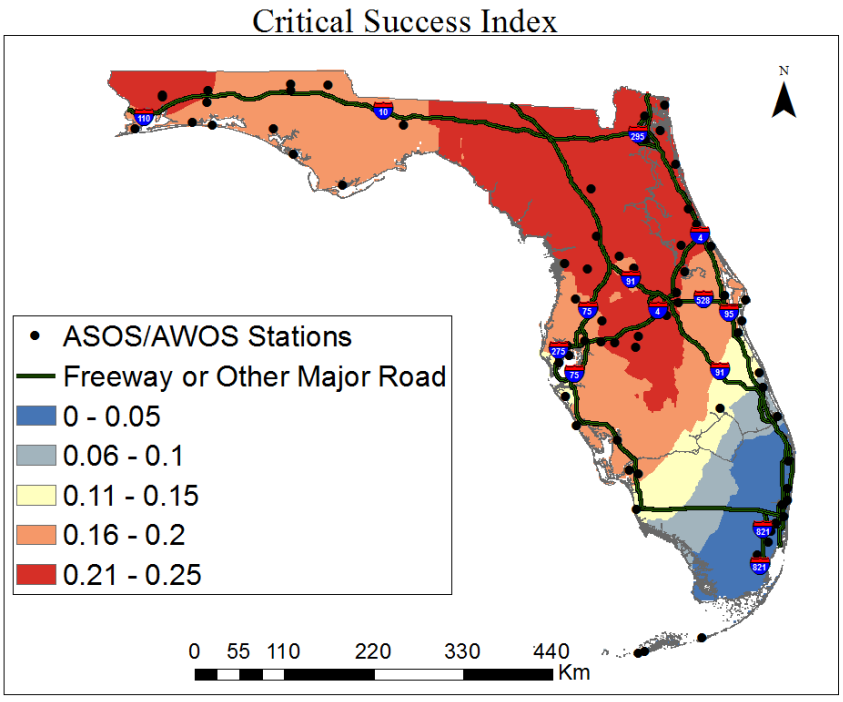

Figure 3.8: Critical Success Index for each individual station plotted and contoured using a GIS Kriging technique. The overall CSI was 0.182 with a station average of 0.15 and a standard deviation of 0.10.

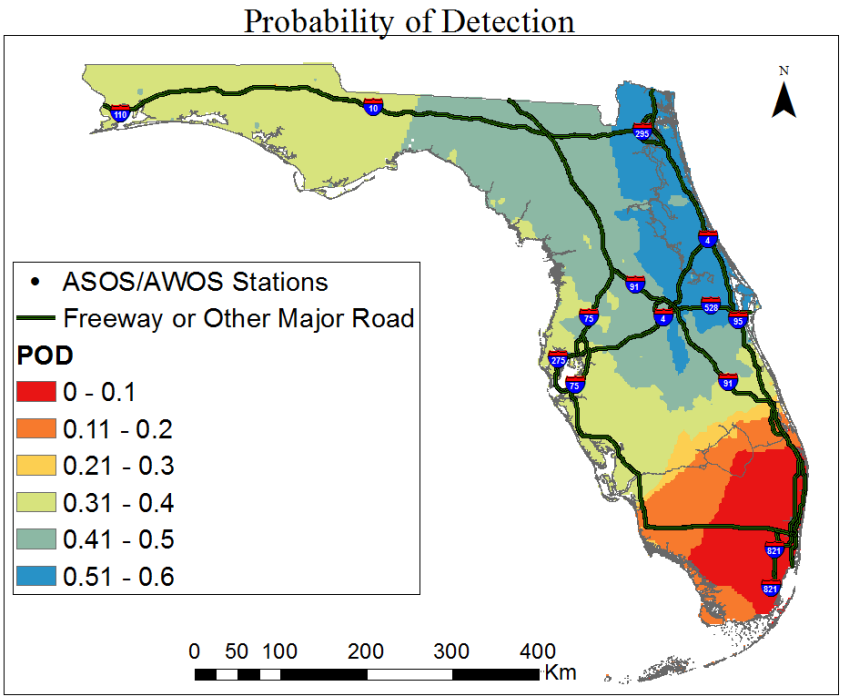

Figure 3.9: Probability of Detection for each individual station plotted and contoured using a GIS Kriging technique. The overall POD was 0.40 with a station average of 0.36 and a standard deviation of 0.24.

3.3.1 RELATIONSHIP BETWEEN SATELLITE AND ASOS/AWOS FOG DETERMINATION

The data gathered at the surface gives us both ground-truth and a way to rectify the satellite data. Given the uncertainties in the satellite data, the surface observations indicate how to properly use and interpret the satellite fog product.

The intercomparison between ground-based point data and the derived satellite fog products for validation can result in a number of uncertainties. As stated earlier, one of the issues is of sub-pixel resolution, in which ground-based point data may not represent the conditions over an entire pixel as seen by the satellite. This may cause ground-based observations to not be detected in the pixel as a whole. This is the case for GOES-8+ IR images where the nominal size of a pixel at sub-satellite point is 4x4 km. At the latitude of

northern Florida, the resolution is a little less than this. This issue becomes apparent when determining the margins of a fog patch or when an observation site is located between two pixels, making it difficult to attribute the data to either one (Cermak and Bendix, 2008). Also, there is a difference in perspective. A satellite image's view from the top and station's visibility measurement from ground level may not agree in some cases.

The other issue with this intercomparison is of temporal scale. GOES Imager takes 15-30 minutes for one scan of the hemisphere, scanning from south to north. The nominal time assigned to an image scene may not actually be the scan time at a given location of that scene. Thus, ground-based observations and satellite images with the same time may not always show the same conditions. Another concern involves co-location errors, which were mentioned previously and are detailed in the appendix. While a manual filtering of the scenes was done to correct the co-registration between the two IR channels, there is always the possibility that geo-location may still be slightly off.

Despite the disadvantages, ground-truth point data is the only data that can be used to compare and validate the satellite fog products. Figure 3.10 shows the percent correct, which is another validation statistic obtained from values derived in the contingency table. As was noted earlier, the skill scores such as CSI and POD does not account for the number of correctly detected non-fog events. Due to the probability of a fog event occurring being small in nature, the number of correctly detected non-fog events is a rather large number. The PC measures the overall accuracy of detecting both fog and non-fog events correctly by weighing both of them equally. The values overall were fairly high for this, with the station average being 87%.

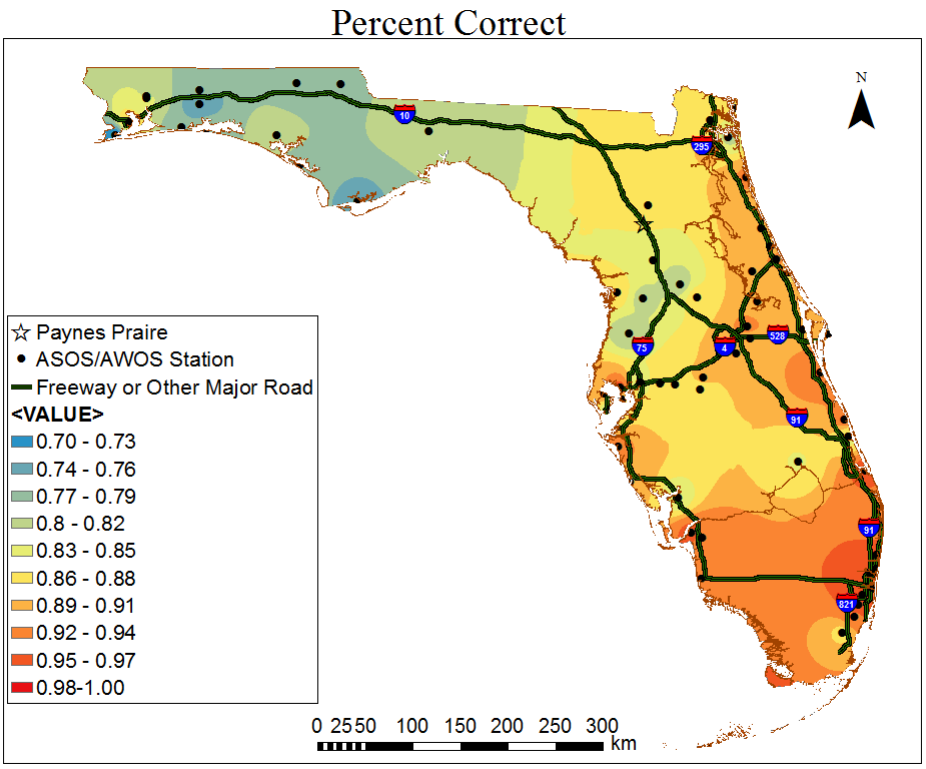

Figure 3.10: Percent correct measured for each station and interpolated using a Kriging function. PC is a measure of overall accuracy.

The bias score is a different type of measure as compared to the CSI/POD/FAR. Those are measures of success while the bias compares the relative frequencies between observed and detected events. It does not measure skill in correspondence. These values are shown in Figure 3.11. The bias scores show that 86% of the stations experienced an over-detection of fog in the validation study. The stations with the largest fog overestimates were mostly located in South Florida and east Central Florida, specifically along Interstate-4 and most of Interstate-95. The most prominent trend is along I-4, which runs east-west through Central Florida. The eastern bound portion intersects a region of large over-detection of fog while the western bound portion intersects a region of large

under-detection of fog. This same pattern is seen in the station fog frequency map, however it depicts a gradual increasing trend of fog occurrences from east to west.

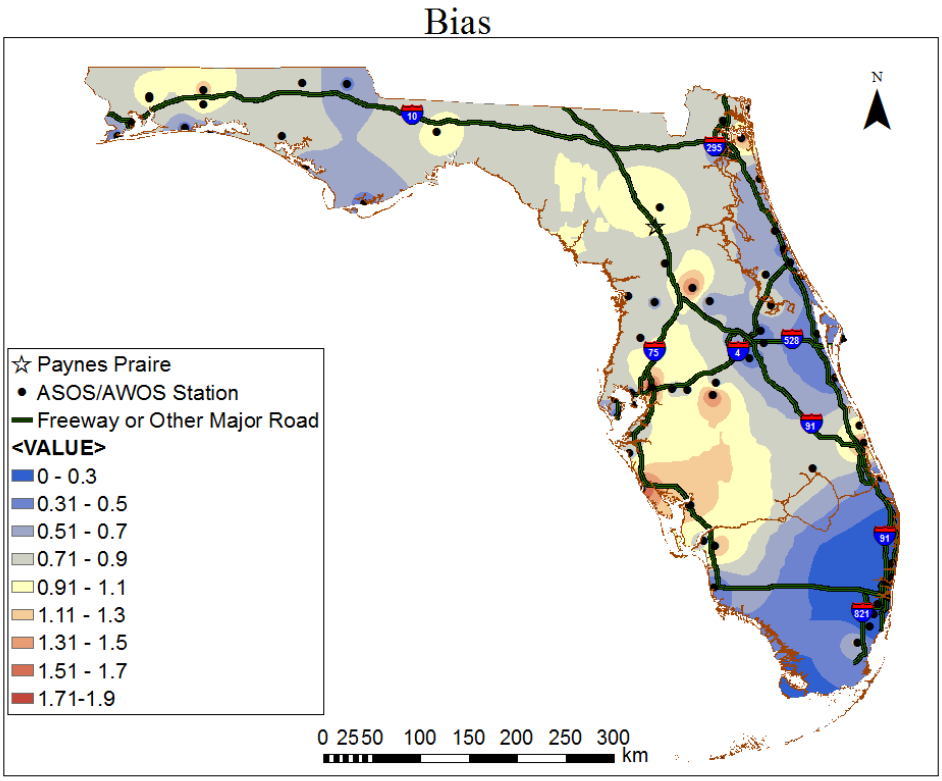

Figure 3.11: Bias Score for each individual station plotted and contoured using a GIS Kriging technique. The overall BS was 0.71 with a station average of 0.68 and a standard deviation of 0.42.

3.3.2 Processing Fog products

After the product validation is complete, the 366 fog images are processed using McIdas software. For each image, each pixel was tested against a certain threshold and classified as either a 1 meaning fog, 0 meaning no fog, or 2 meaning high cirrus cloud. These pixel classifications were saved in a separate array for each image.

The GOES-13 images are all of the same size and have the same boundary coordinates. The image dimensions are 568x208, which makes 118,114 pixels per image. The spatial extent covers approximately 90.483°W-75.910°W and 32.183°N-22.931°N. Therefore, it spans 14.58° longitude and 9.25° latitude. GOES Imager data has twice the sampling resolution in the horizontal direction compared to the vertical direction. Therefore, each pixel represents roughly 0.025 x 0.044 decimal degrees.

Once the fog images for the year were classified, the annual and seasonal sums of fog occurrence were computed for each pixel. Seasonal and annual arrays made up of fog frequencies for each pixel was obtained. This was done for cirrus events as well. The pixels were plotted in ArcGIS and converted into a raster grid using the navigational coordinates of the image. The cell sizes for the raster grids in GIS can only be of equal length and width. Because of this, a cell size of 0.05132 was specified to fit the image size dimensions. Thus, the grid displaying satellite fog frequency is of slightly lower resolution and aggregates roughly two pixel values from the satellite image to map the fog frequency for one cell on the grid.

GOES-13 and GOES-14 images were both utilized in this study due to a short GOES-13 outage. This occurred in the fall season; 25 out of the 366 days were obtained from GOES-14. This did not affect the quality of the data. The only slight predicament was due to varying image sizes in the GOES-14 images. Therefore, they had to be processed and summed separately within ArcGIS due to a difference in total number of pixels as well as navigational points. Nonetheless, GIS provided a simple way to combine the GOES-13 and GOES-14 data geospatially.

3.3.3 Climatology of adding satellite data

Averaging of the satellite fog products was performed for seasonal and annual periods. For each pixel, the frequency of fog was obtained and plotted on a 5x5-km grid, as described in the previous section. The annual fog frequency as detected by the satellite is shown in Figure 3.12. There is a clear over-detection of fog from the satellites. However, this was expected considering the fog algorithm is not able to differentiate between fog and low cloud cases. Overall, there is no distinct geographic variation of fog in the satellite-derived map as was seen in the interpolated station data map. While the fog event minimum is still located in the southeastern tip of Florida, the fog event maximum in North Florida as given by the station reports is not resolved. Instead, the fog product detects between 40-70 fog events for the majority of the state.

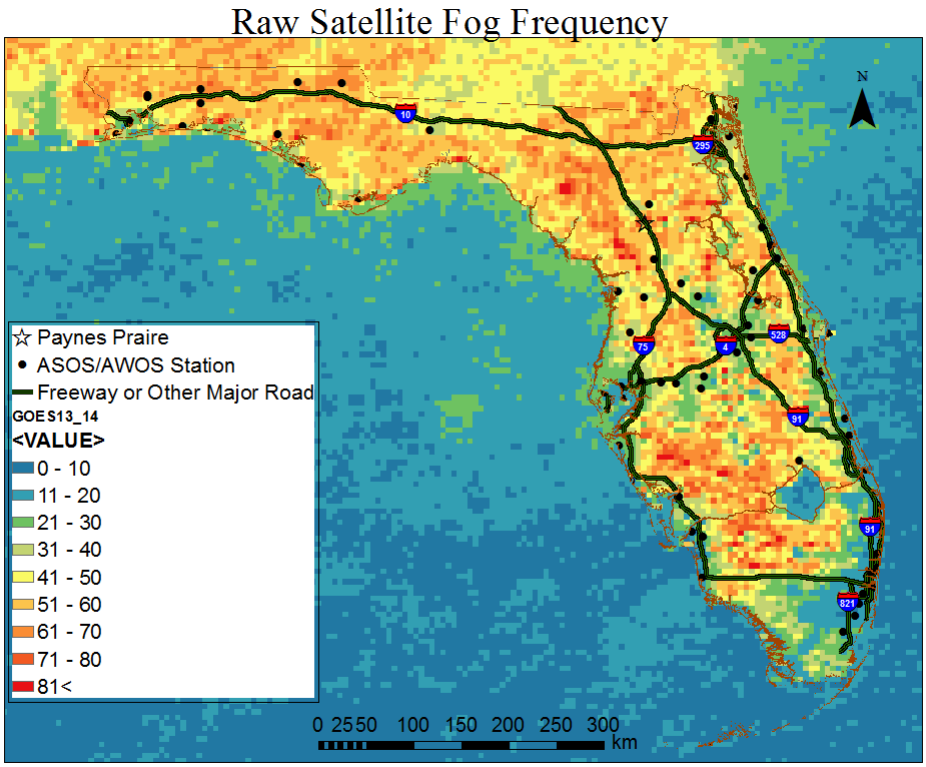

Figure 3.12: Annual number of fog days for the year 2012 as observed by the GOES fog product.

3.3.4 Calibration of Satellite data

To avoid known biases, the satellite data was calibrated based on the known performance of the satellite fog detection scheme at the station sites. The bias was used as the adjustment factor and represents the ratio between the number of fog events the station reported versus the number of fog events the satellite detected at the same location. The bias error at each station site was interpolated using an inverse distance weighting technique. This generated a layer of bias errors that was used to adjust the raw annual fog frequency map derived from the satellite data. The results are shown in Figure 3.13.

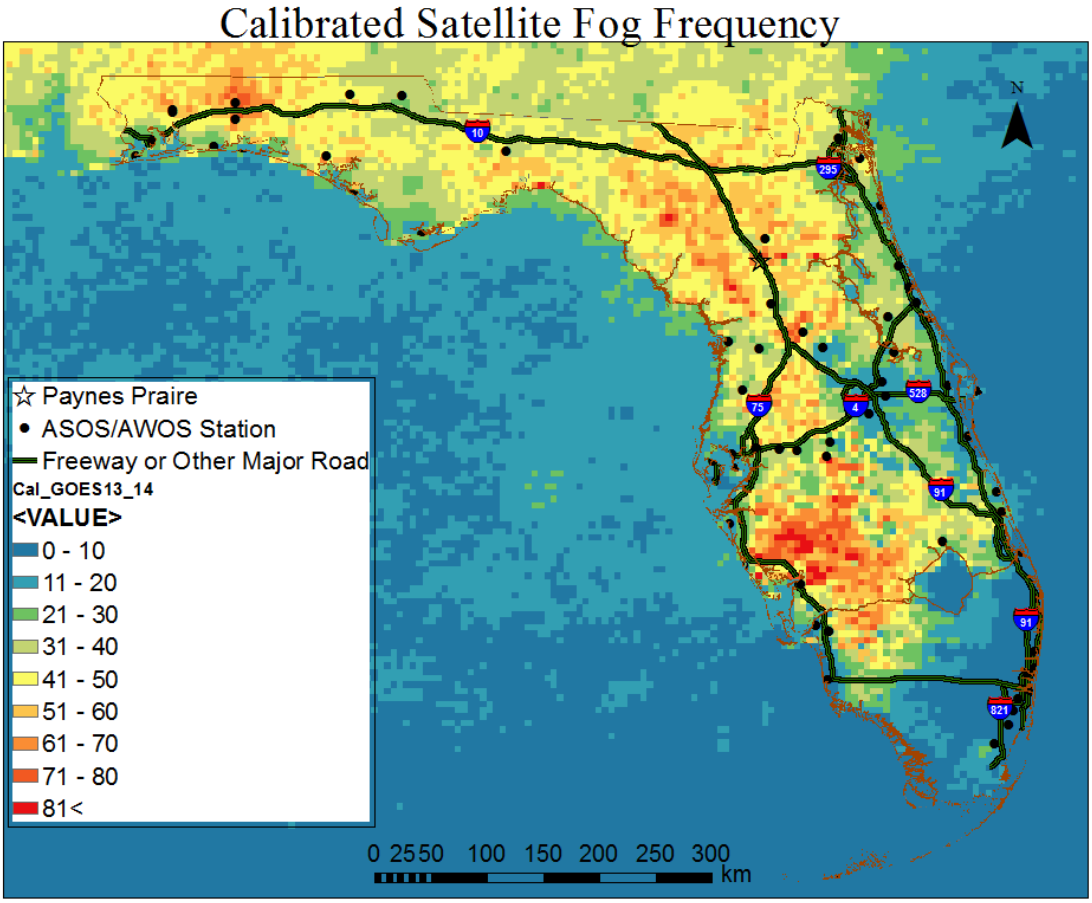

Figure 3.13: Adjusted GOES satellite image of fog frequency for 2012.

Correcting for known errors of under-detection and over-detection based on measures from the validation study produces a more realistic result. The calibrated annual fog frequency displays greater similarities in spatial patterns with the station-interpolated map shown in Figures 1.2 and 2.1.

The adjusted satellite map was compared to the interpolation of fog events observed at the stations using an ordinary least squares regression. The standardized residuals are obtained and plotted in Figure 3.14. A portion of the pixels falls outside of ±2.5 standard deviations, suggesting possible errors and outliers in the fog algorithm results. This negative bias corresponds with the location of maximum fog occurrences south west of I-4 as seen on the adjusted-satellite map. While it's possible that this is an outlier, more data is needed to attest this.

A correlation of r= 0.686 was found between the satellite and station fog counts. Since the fog product's performance is both scaled and compared to data derived through interpolation of the ground observations, some amount of error is anticipated. This is largely due to the low density of ground observations. However, knowing the location and magnitude of these errors can indicate how to correct for them in the future. According to the standardized residuals map, the positive biases cluster in the panhandle and in coastal areas while the negative biases are prominent in south Florida and parts of central Florida. Regional differences in fog detection performance may unveil variable conditions involving fog tendencies.

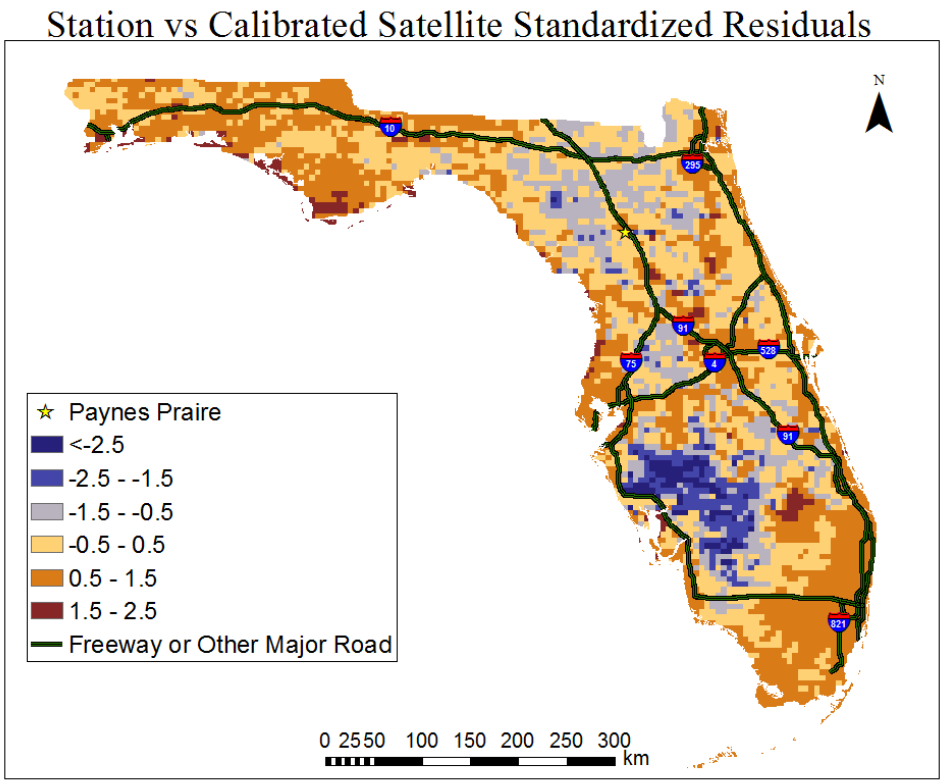

Figure 3.14: Calculated standardized residuals from ordinary least squares test between the station observed fog and the scaled-satellite observed fog,

3.3.5 RELATIONSHIP BETWEEN CLOUDS AND FOG DETERMINED BY SATELLITE OBSERVATIONS

The amount of fog reported by the satellite represents the amount not obscured by higher clouds. Removing the high cloud contamination from the contingency statistics earlier in the study increased the skills scores such as POD and CSI, suggesting that a significant number of missed fog cases may be attributed to multi-layer cloud cases (Cermak and Bendix, 2008). Situations in which overlying clouds are present can lead to faulty computations of fog occurrences. The simplest way in compensating for this is by assuming that the frequency of fog is the same as when it's obscured to when it's not obscured. Conversely, there may be a correlation between the occurrence of fog and high clouds where the frequency of fog is different because of high cloud layers abstaining fog (Hahn and Warren 2007). To test for this, the frequency of occurrence of high-level clouds can be plotted against the frequency of occurrence of fog.

The frequency of high clouds in 2012 is shown in Figure 3.15. A quick visual comparison between this map and the satellite-derived fog frequency map shows evidence of some corroboration. For instance, fog events were minimal in South Florida near Miami while high cloud events were at a maximum. Likewise, in places where the fog frequency was relatively high, the high-cloud frequency was relatively low (for example, in the small region southwest of Paynes Praire). The presence of cloud absorbs both heat and aerosols, which can reduce the chances of fog formation (Saraf et al., 2010). A strong negative correlation (r=-0.81) was found in comparing the annual occurrence of fog with the annual occurrence of high cloud per pixel. Defining cloud cover trends as it relates to fog rates requires further investigation.

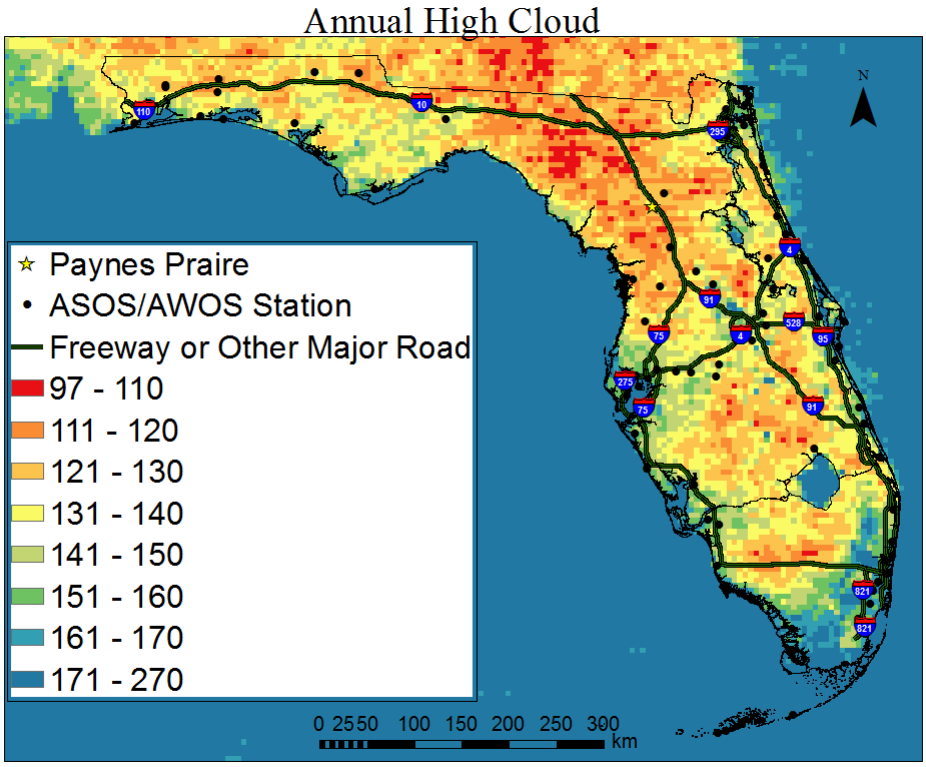

Figure 3.15: Number of times satellite detected a high cloud at each pixel in 2012. The number reflects the number of days out of 366 possible days. A strong negative relationship is seen between the occurrence of high clouds and the occurrence of fog,

3.4 SUMMARY OF CLIMATOLOGY

The scaled satellite fog frequency map demonstrates similar features seen in the one-year and 5-year of ground observed fog (Figures 2.1 and 1.2 respectively). The average number of fog events after the scaling of the satellite data was 35 with a standard deviation of 18 over the state of Florida. While the magnitude of fog frequency is greater in the satellite-derived map, the spatial patterns agree fairly well with the patterns seen from the station data. Figure 3.16 shows the scaled satellite image with the station reported fog frequency contours superimposed. The distribution of fog events as detected by the satellite emulates the fog event trends based on ground observation fairly well.

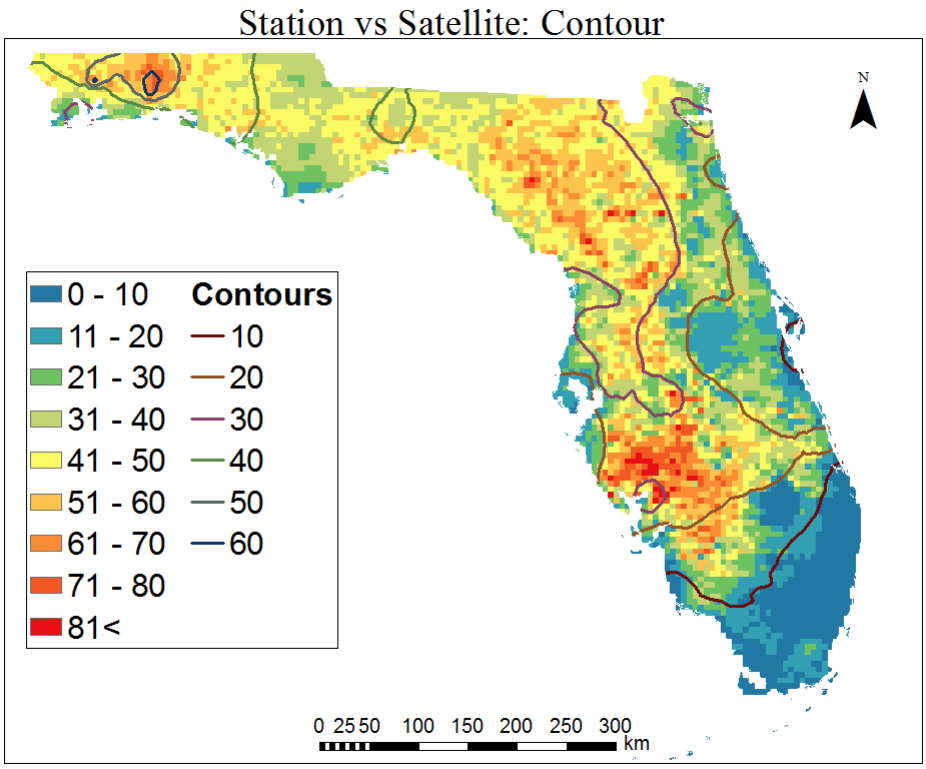

Figure 3.16: Calibrated satellite fog frequency with contours of the observed fog frequency at the stations overlay.

3.4.1 MONTHLY AND SEASONALLY

The monthly average fog occurrences as reported by ASOS/AWOS sites and as detected by satellite are shown below in Figure 3.17. The monthly distribution agrees with previous studies showing January and December as the peak fog months. However, the fog product shows December and November as the peak fog months and February having more fog events than January. The stations observed more fog than were detected during the warmer months between May and September. The number of agreements (hits) between station reports and satellite detection varies similarly with more occurrences during the cool months and hardly any in the summer months.

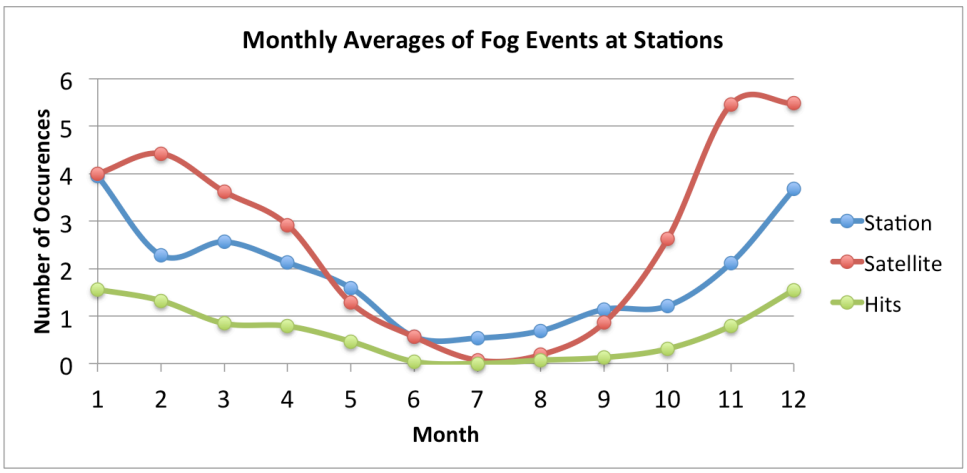

Figure 3.17: Mean fog frequency at the stations per month. The totals observed from both ASOS/AWOS sites and satellite algorithm are both plotted. The average amount of hits, or matches between the two from the stations is shown as well.

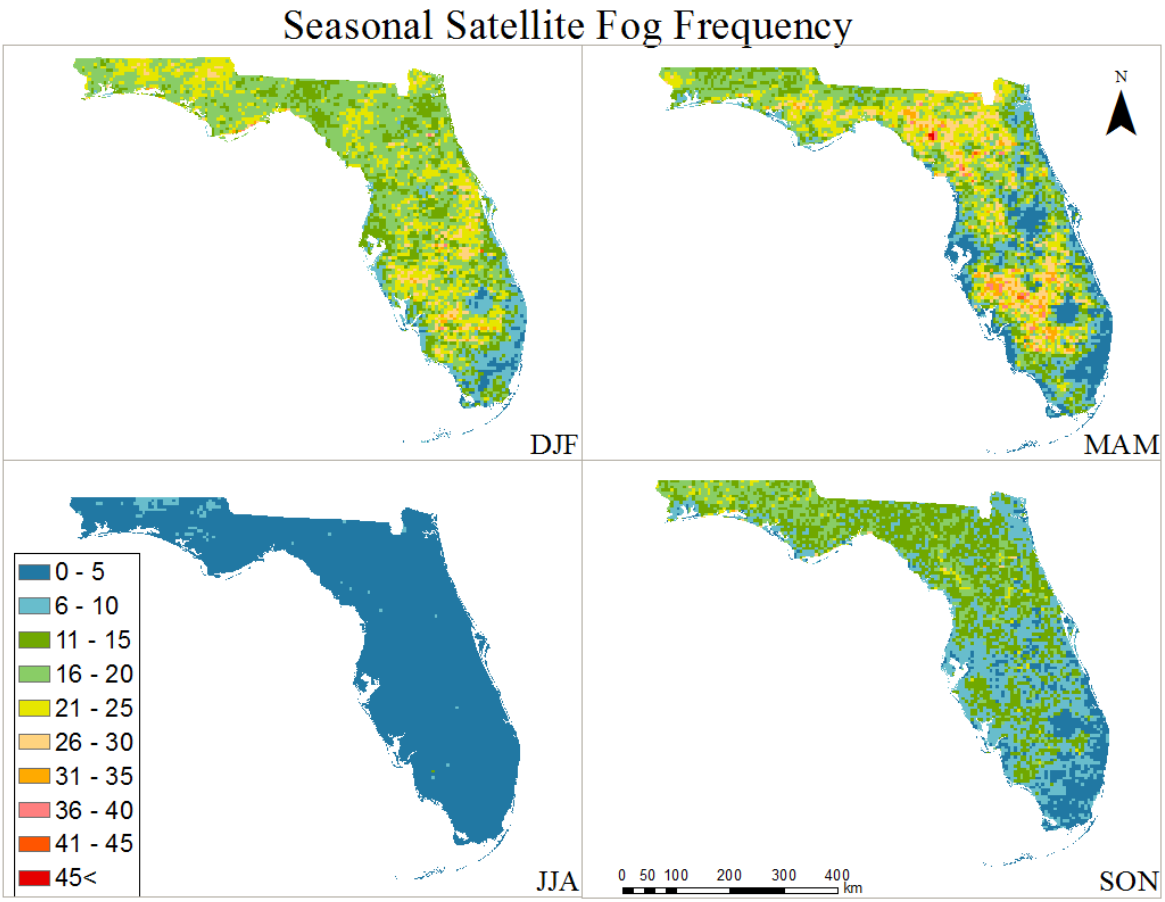

Figure 3.18: Seasonal fog occurrences as detected by raw GOES fog product.

Seasons were defined as winter (DJF), spring (MAM), summer (JJA) and fall (SON). The fog products were separated by season and summed accordingly. Figure 3.18 shows the seasonal fog frequency. These seasonal images are not scaled; they represent fog amount estimates based on raw satellite data. As noted from the monthly totals, the summer months had minimal fog occurrences across the majority of the state. The few pixels where fog was more frequent are mostly in the northern panhandle. Interestingly, the maximum number of fog events does not occur during the winter months as expected, but occurs during the spring. The satellite seasonal averages for spring and winter are 16 and 17 with standard deviations 7 and 6, respectively. The spring months display much more spatial variation as compared to the winter months.

The station-satellite residuals were calculated seasonally for each station. These biases were then interpolated at all pixel locations. The seasonal interpolated biases were then added to the raw satellite maps. The seasonal biases and adjusted maps are shown in Figures 3.19 and 3.20 respectively.

Winter and fall show the largest biases. The residual differences for winter, spring and fall depict the same general over-estimation of fog from the fog product. However, the summer months are an exception and fog events are under-estimated, specifically in the panhandle region.

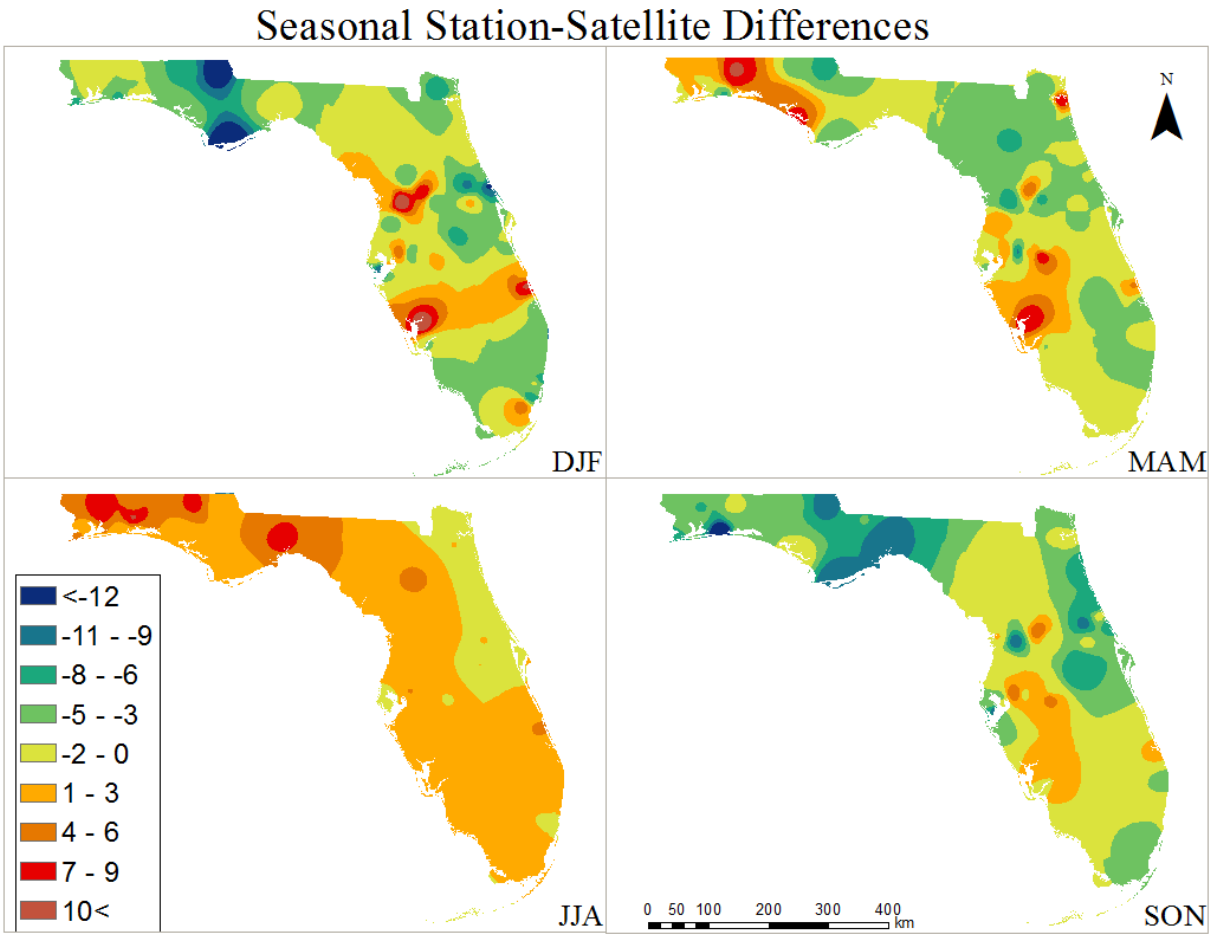

Figure 3.19: Seasonal station-satellite differences (bias). The values at station locations are interpolated at all station pixels using inverse distance weighting technique.

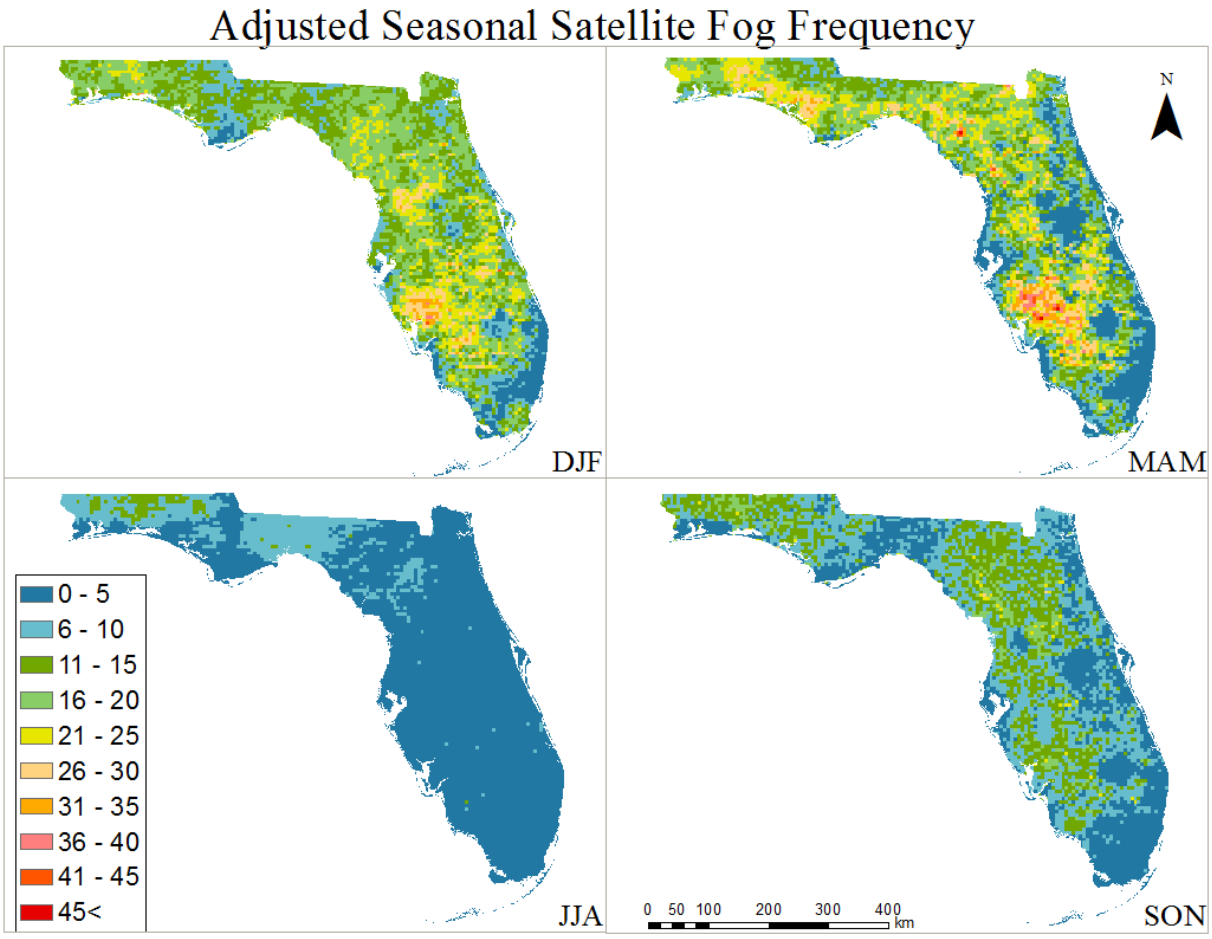

Figure 3.20: Adjusted seasonal fog occurrences as detected by GOES fog product.

3.4.2 ANNUALLY

There is a decreasing trend of fog occurrences from north to sound and from the west coast to the east coast. However, the satellite shows a pronounced maximum of fog events in the region around Tampa. Station data is extremely sparse within this region, making it difficult to verify whether the interpolated station map or satellite-derived map is more accurate.

Regional stratification was done on the satellite data in terms of an elevation layer of 1-km resolution (obtained from U.S. Geological Survey (USGS) National Elevation Map). Florida is mostly flat with a ridge of relatively higher elevations in the central part of the state. The elevation data was divided into 5 equal interval zones based on height. The zonal histogram in Figure 3.21 shows the distribution of fog frequency within each of these zones. There appears to be a strong positive relationship between the topography and number of fog events, with the frequency gradient matching the locations of rising elevation. This is especially true in the western portions of Florida and occurs in the same region of the fog 'hot-spot' seen in the satellite images. This apparent correlation can be explained by the mechanics of upslope or frontal fog. As warm moist air from the Gulf of Mexico moves over cooler land surfaces, slightly upslope terrain can act as the forcing mechanism that cools the temperature to its dew point. This has been known to occur especially on western-facing slopes (Peace, 1986). It may be of interest to further monitor this region for fog occurrences and assess whether these observations are valid.

There was also a strong relationship between the satellite fog frequency map and a 2006-2010 fog-related crash density map. Florida ranked third in highest number of fog/smoke related accidents in the US between 2003-2007 (Abdel-Aty et al. 2012.). Figure

3.22 (obtained from Ray et al., 2014) depicts crash densities as a function of both occurrence and population. It illustrates the quantity of accidents that have occurred in certain areas. These locations tend to be in low-lying, coastal and metropolitan areas, with high levels of crash density along the I-4 highway corridor. The region where the satellite detects the maximum number of fog (southwest of I-4) appears to have had a sizeable number of fog-related accidents occur there.

In the early morning hours of January 9, 2008, drivers traveling on I-4 by Polk County faced a mixture of dense fog and smoke that resulted in a seventy car and truck pile-up. This resulted in 38 injuries and 5 deaths. The terrain in this region is nearly flat with some slight rises and swampy sinks which increase micro-scale relative humidity, making it favorable for fog formation (Collins and Paxton, 2009). Due to station data being sparse and GOES not being able to fully resolve mesoscale fog events with certainty, it has been suggested that environmental roadway sensors be installed to detect and inform officials of low visibilities quickly (Ellrod and Lindstrom, 2006). This would be useful in the regions where GOES detected high fog frequencies and would aid in future fog remote sensing assessments.

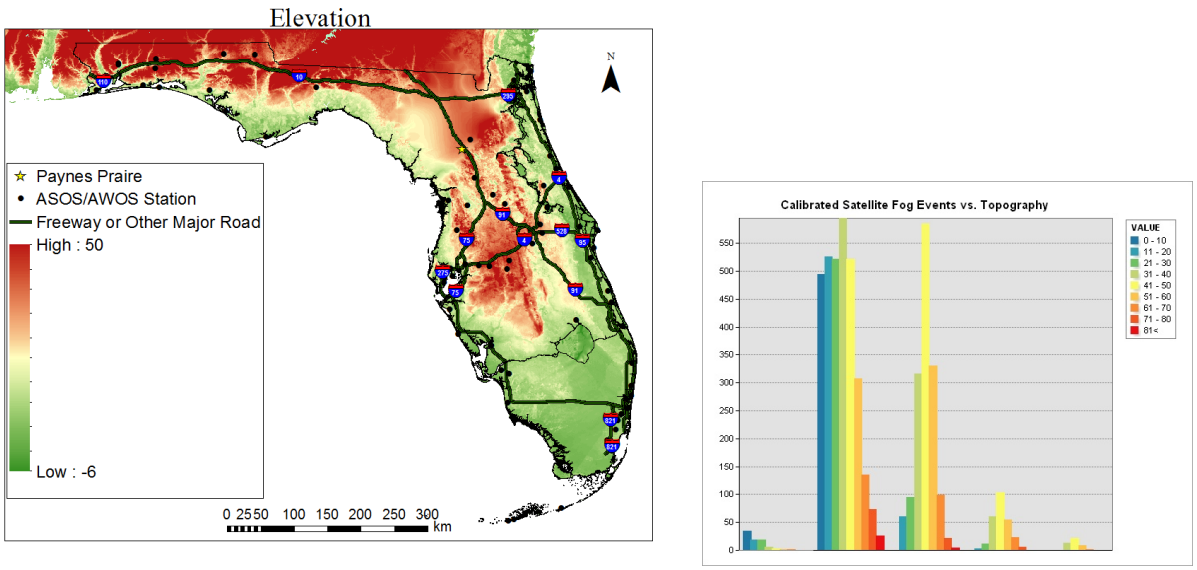

Figure 3.21: On the left is the USGS DEM elevation map for Florida. This map was broken into 5 groups of equal elevation intervals. The zonal histogram for each of these is shown in the bar graphs on the right.

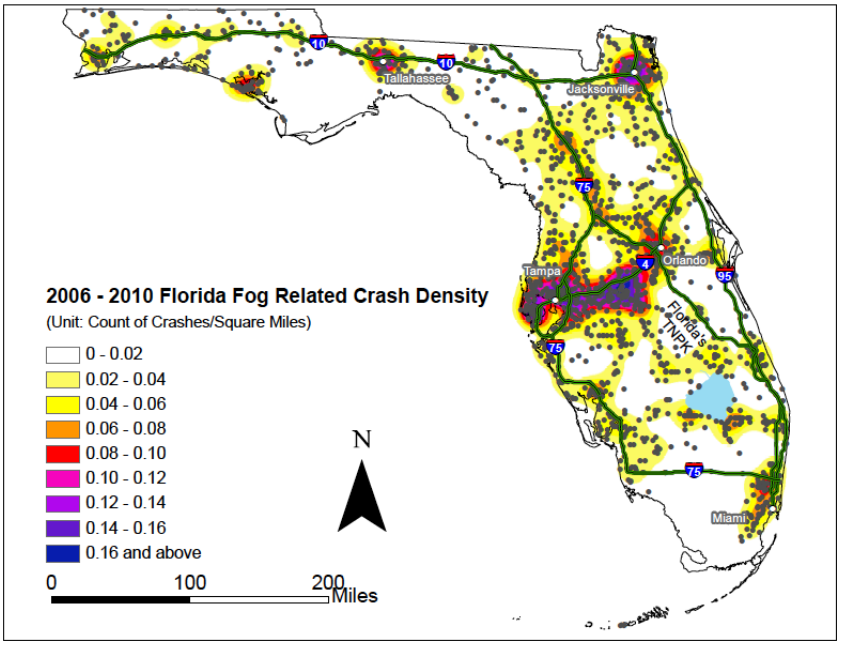

Figure 3.22: Fog and smoke related crash density for 2006-20110. Units are in crashes per square mile. Data from Department of Transportation (DOT) accident reports and figure obtained from Ray et al. (2014).

CHAPTER FOUR

SUMMARY AND CONCLUSIONS

The use of two infrared channels on GOES-13/-14 did show modest skill in detecting fog. One of the principal weaknesses was due to fog processes being of sub-pixel resolution in satellite imagery. This, along with obstructing cloud layers contributed to the large amount of satellite misses. The false alarms can be attributed to the fog algorithm not being able to decipher between fog and stratus clouds. The large number of non-fog events compared to fog events suggests that the use of a BTD threshold was not enough and further classifiers may be necessary to distinguish fog. For example, progress has been made in distinguishing between low cloud and fog by incorporating surface temperature data with the GOES imagery (Ellrod, 2002). As was mentioned previously, the fog product does not resolve fog situations under overlying clouds. Future efforts focused on how to better utilize ground-based data and satellite-based data simultaneously may help remedy this problem. Another limitation includes the short one-year time period that was used to define a fog 'climatology' and validate a fog algorithm. Future studies would benefit from using multi-year datasets. Analyzing multiple images throughout the morning hours would also be useful in better understanding not just the spatial extent of fog but also fog development.

Even though the algorithm generally over-estimated fog amounts, the spatial patterns were similar to those perceived in past climatologies. The satellite-derived

annual/seasonal patterns and spatial variations in bias errors suggest that the optimum fog BTD threshold may vary with season and location.

Improvements will be made by the next generation of geostationary satellites that will replace the current GOES satellite series, which features an Advanced Baseline Imager (Schmit et al. 2005). With four times the spatial resolution, additional bands, increased coverage and improved image navigation, the fog product's performance is expected to improve significantly. A simulated GOES-R fog product is illustrated in Figure 4.1 using MODIS imagery.

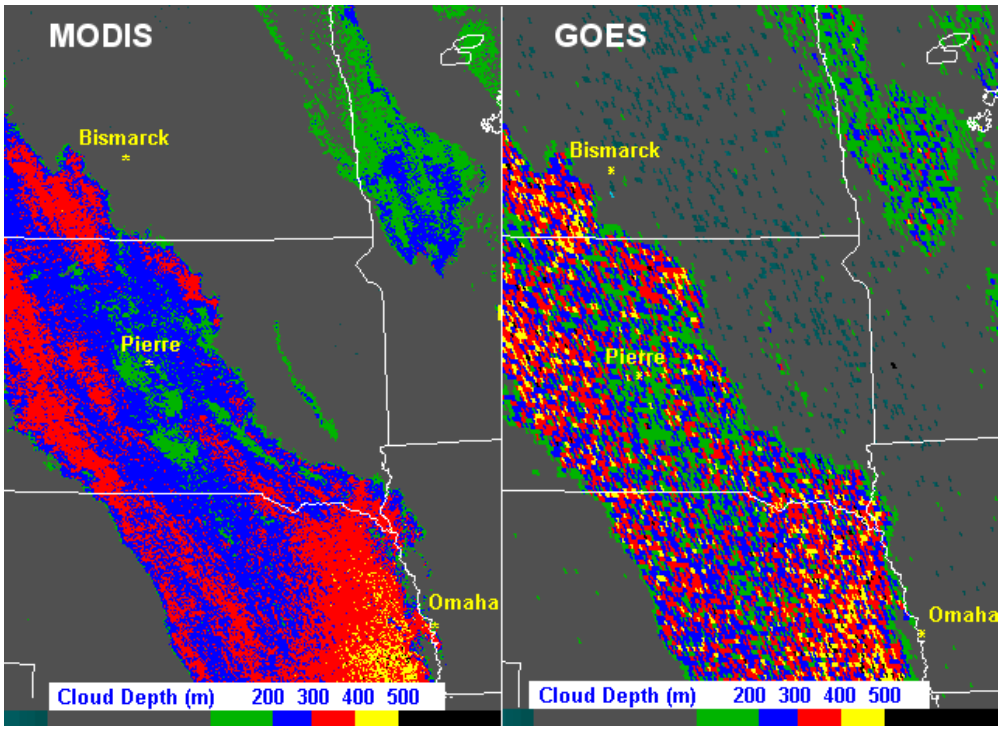

Figure 4.1: Fog depth image enhancement simulation from 1km resolution MODIS (left) versus current 4km GOES (right) (From Ellrod, G. P. and S. Lindstrom, 2006.)

Even though the fog algorithm showed moderate skill, the main objective was fulfilled; to delineate the zones and areas in between ground observation data that may be prone to fog. Implementing GIS as a tool for multi-parameter analysis helped infer correlations between fog and local topographic and physical features. Regardless, a spatially continuous map of fog events in Florida developed from both satellite and ground observation data delivered promising results. The value of this satellite-derived fog detection method is to provide a more comprehensive spatial view of fog by improving the estimates of fog between ASOS/AWOS sites.

APPENDICES

APPENDIX A

TABLE A1. COORDINATES OF THE ASOS AND AWOS STATIONS

Number	Station ID	Name	Longitude	Latitude
1	1J0	Bonifay Tri CO	-85.6014	30.8458
2	2J9	Quincy	-84.5574	30.5979
3	AAF	Apalachicola Muni	-85.0274	29.7276
4	APF	Naples Muni AP	-81.7753	26.1525
5	BKV	Brooksville	-82.4544	28.4736
6	BOW	Bartow Municipal	-81.7834	27.9434
7	CEW	Crestview	-86.5200	30.7800
8	CGC	Crystal River	-82.5713	28.8673
9	COF	Patrick AFB/Cocoa Beach	-80.6100	28.2350
10	CRG	Jacksonville Craig Muni AP	-81.5147	30.3361
11	DAB	Daytona Beach Intl	-81.0581	29.1799
12	DED	Deland	-81.2837	29.0670
13	DTS	Destin Ft Walton	-86.4700	30.4000
14	ECP	Panama City	-85.7956	30.3582
15	EGI	Duke FLD/Eglin	-86.5229	30.6503
16	EVB	New Smyrna Beach Muni	-80.9489	29.0557
17	FHB	Fernandina Beach	-81.4612	30.6118
18	FLL	Ft Lauderdale Hollywood AP	-80.1500	26.0700
19	FMY	Ft Myers Page FLD AP	-81.8615	26.5849
20	FPR	Ft Pierce St Lucie Co Intl AP	-80.3766	27.4981
21	FXE	Ft Lauderdale Executive AP	-80.1700	26.2000
22	GIF	Winter Haven Gilbert AP	-81.7533	28.0629
23	GNV	Gainesville Rgnl AP	-82.2760	29.6917
24	HRT	Hurlburt Field (AF)	-86.6893	30.4278
25	HWO	Hollywood North Perry AP	-80.2412	25.9995
26	ISM	Kissimmee Muni Airport/Orlando	-81.4400	28.2900
27	JAX	Jacksonville Intl AP	-81.6879	30.4941
28	LAL	Lakeland Regional	-82.0186	27.9889
29	LEE	Leesburg Muni AP	-81.8100	28.8200
30	MAI	Marianna Muni AP	-85.1839	30.8356

31	MCF	Macdill AFB/Tampa	-82.5200	27.8500
32	MCO	Orlando Intl AP	-81.3090	28.4294
33	MIA	Miami Intl AP	-80.3169	25.7880
34	MLB	Melbourne Intl AP	-80.6453	28.1028
35	MTH	Marathon AP	-81.0514	24.7262
36	NDZ	Milton/Whiting Field NAS South	-87.0231	30.7044
37	NIP	Jacksonville NAS	-81.6747	30.2342
38	NPA	Pensacola NAS	-87.3180	30.3533
39	NQX	Key West NAS	-81.6888	24.5757
40	NSE	Whiting Field NAS-N	-87.0219	30.7242
41	OBE	Okeechobee	-80.8498	27.2628
42	OCF	Ocala Muni (ASOS)	-82.2242	29.1726
43	OMN	Ormond Beach Muni	-81.1136	29.3006
44	OPF	Miami Opa Locka AP	-80.2828	25.9102
45	ORL	Orlando Executive AP	-81.3329	28.5455
46	PAM	Tyndall AFB	-85.5754	30.0696
47	PBI	West Palm Beach Intl AP	-80.0994	26.6847
48	PCM	Plant City	-82.1642	28.0002
49	PGD	Punta Gorda Charlotte CO AP	-81.9914	26.9172
50	PIE	St Petersburg Intl AP	-82.6874	27.9100
51	PMP	Pompano Beach Airpark	-80.1110	26.2464
52	PNS	Pensacola Rgnl AP	-87.1869	30.4781
53	RSW	Ft Myers SW FL Rgnl AP	-81.7567	26.5381
54	SFB	Orlando Sanford AP	-81.2436	28.7797
55	SGJ	St Augustine	-81.3397	29.9593
56	SRQ	Sarasota Bradenton AP	-82.5586	27.4014
57	SUA	Whitham Field Airport/Stuart	-80.2200	27.1800
58	TIX	Titusville	-80.7992	28.5148
59	TLH	Tallahassee Rgnl AP	-84.3513	30.3935
60	TMB	Miami Kendall Tamiami Exec AP	-80.4347	25.6423
61	TPA	Tampa Intl AP	-82.5403	27.9619
62	VDF	Vandenberg Airport/ Tampa	-82.3453	28.0140
63	VNC	Venice	-82.4403	27.0716
64	VRB	Vero Beach Intl AP	-80.4179	27.6556
65	VVG	The Villages	-81.9701	28.9444
66	XFL	Palm Coast	-81.2063	29.4674
67	XMR	Cape Canaveral	-80.5668	28.4677

68	BCT	Boca Raton Airport	-80.1100	26.3800
69	EYW	Key West	-81.7596	24.5561
70	INF	Inverness	-82.3182	28.8036
71	SPG	Saint Petersburg	-82.6270	27.7651

APPENDIX B

TABLE B1. SURFACE OBSERVATION SITE INSTRUMENTATION

- Ceilometer, Cloud Height Indicator [CHI] Sensor (one to three sensors per site)
- Visibility Sensor (one to three sensors per site)
- Precipitation Identification (PI) Sensor
- Freezing Rain (ZR) Sensor (not included where ZR potential is nil)
- Lightning Sensor (only at selected sites)
- Pressure Sensors (two sensors at small airports; three sensors at larger airports)
- Ambient/Dew Point Temperature Sensor
- Anemometer (wind direction and speed sensor)
- Precipitation Accumulation Sensor (Heated Tipping bucket)

APPENDIX C

TABLE C1 CHARACTERISTICS OF THE GOES-13 SATELLITE

GOES Imager Band	Wavelength Range (μm)	Central Wavelength (μm)	Nominal Subsatellite IGFOV (km)	Meteorological Uses
1	0.55 - 0.75	0.63	1	Daylight cloud cover and surface features
2	3.8 - 4.0	3.9	4	Fog and cloud cover Fire detection
3	6.5 – 7.0	6.48	4	Water vapor
4	10.2 – 11.2	10.7	4	Earth and cloud images; sea surface temperature and water vapor
5	11.5 – 12.5	12.0	4	Cloud cover and cloud height
6	12.9 – 13.7	13.3	4	CO_2 band, Cloud detection

TABLE C2 GOES-13(-EAST) IMAGER SCAN SECTORS IN ROUTINE MODE

Frame Name	Boundaries	Duration (mm:ss)	Scan Times (UTC)
Full Earth	Earth Edge	26:16	0245, 0545, 0845, 11:45, etc
Extended Northern Hemisphere	20°S-66°N 45°W-120°W	14:16	xx15, xx45
Southern Hemisphere	20°S-50°S 30°W-120°W	4:53	xx10, xx40
CONUS	14°N-60°N 60°W-125°W	4:45	xx00, xx30

APPENDIX D

CONVERSION OF GVAR INFRARED DATA TO SCENE RADIANCE OR TEMPERATURE

There are three intermediate steps involved in the conversion of GOES infrared 10-bit GVAR counts into 8-bit brightness counts.

The first step is converting the 10-bit GVAR counts (ranging from 0-1023) to infrared radiances according to the following linear equation:

$$R = (X_g - b)/a$$

where R is radiance in mW/(m^2 sr cm^{-1}), X_g is the GVAR count value (10-bit=2^{10}=1024), and coefficients a and b are scaling slope and intercept which are each band dependent. They are also expected to be constant in time and for each GOES satellite.

GOES Band	a	b
2	227.3889	68.2167
3	38.8383	29.1287
4	5.2285	15.6854
6	5.5297	16.5892

The second step is converting the radiance to effective temperature using the inverse Planck function:

$$T_{eff} = \frac{c_2 n}{\ln\left[1 + \left(\frac{c_1 n^3}{R}\right)\right]}$$

c_1= 1.191066x10^{-5} [mW/(m^2-sr-cm^{-4})]

c_2= 1.438833 (K/cm^{-1})

where T_{eff} is the effective temperature and in degrees Kelvin and accounts for slight variations of the Planck function across the spectral passband of the channel, R is the radiance, c_1 and c_2 are radiation constants and are invariant, and n is the central wavenumber of the channel and is dependent on the spectral channel and instrument. The effective temperature is then converted to actual temperature using:

$$T = \beta \cdot T_{eff} + \alpha$$

Channel	n	α	β
2	2561.74	-1.437204	1.002562
4	937.23	-0.386043	1.001298

where α and β vary with band, detector and instrument. The differences between T and T_{eff} values increase with decreasing temperatures and are of the order of 0.1K approximately. This means that for a 300 K scene, one GVAR count increment is equal to approximately 0.11 K temperature increment in channels 2 and 4.

The final step is to convert temperatures to an 8-bit scale also known as Mode-A, ranging from 0 to 255 brightness counts (or brightness temperatures). Mode-A counts are derived from the temperature values using the following equations (Bristor, 1975):

$$For\ 163K\ \leq T \leq 242K, \qquad X_a = 418 - T$$

$$For\ 242K\ \leq T \leq 330K, \qquad X_a = 660 - 2T$$

This conversion inverts the intensity so that the warmest 88K are displayed as the first 176 counts, the coldest 80K are displayed as the last 80 counts and typical scene temperatures between 220K and 300K are displayed in the middle grey levels. The above scaling is usually done for display purposes and provides more precision at the warmer end of the spectrum (1 count = 0.5K).

For the best precision, temperature values converted from 10-bit counts are used for calculating the fog product.

APPENDIX E

RESAMPLING TO IMPROVE CO-REGISTRATION

All channels are collected at the same time. But for some reason they are not co-registered. That means that they do not overlay one another exactly. For such a local phenomena as fog, this would render the fog algorithm, which relies on the brightness difference between two channels, useless. It simply must be corrected. Exacerbating the problem is that for a period of a month or so, when GOES 13 was inoperative, GOES 14 was employed, and the apparent registration error was spatially in the opposite direction. The difference is of the order of one-two pixels, but that is significant.

This problem was discovered in looking at the brightness differences and noting that one edge (left or right) was either bright or dark and the other edge exhibited the opposite brightness. Also the contrasting brightness was visible in how the coastlines were rendered. Figure E1 shows maps with fog/low cloud enhancement on CH-4-CH-2 temperature difference images for November 4, 2012 at 11:15 UTC before correction and

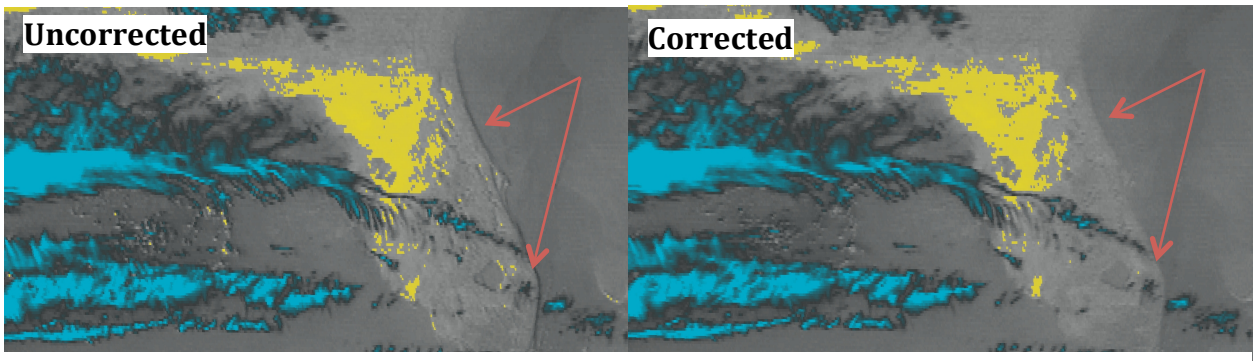

Figure E 1 Fog products for November 4, 2012 11:15 UTC before and after correction of CH-2. Artifacts in the uncorrected image are shown along the eastern coast of Florida. False positives are also shown along the eastern boundary of Lake Okeechobee in the uncorrected image. The corrected fog product image consists of the corrected Ch-2 Image, which was resampled and shifted east by 0.824706 pixels.

after correction of CH-2. Forty ASOS/AWOS sites reported fog during the early morning hours. The asymmetric behavior is seen along the eastern coastline of Florida. Surface features, such as Lake Okeechobee appear smoother in the corrected image. Also, there is a fog signal along the eastern boundary of Lake Okeechobee in the uncorrected image. However, the corrected image shows that these are artidacts caused by larger co-registration erros which lead to a false positive in fog detection.

Although a first order correction is possible with a simple east-west shift, a more sophisticated approach that allows for sub pixel resampling is to use a Fast Fourier Transformation Resampling algorithm (FFTR). The procedure is described in Li *et. Al* (2014). This approach does not use a set of fixed points to establish the adjustment, but rather an area approach, which maximizes the correlation between two images through their Fourier transforms. Without this correction, it is likely to increase the number of false positives in the fog detection algorithm.

The principal aspect is to do a line-by-line cross correlation between Channels 2 and 4. The phase shift that maximizes the correlations (only over land) is saved along with the cross-correlation coefficient for each line. Then the weighted (by the correlation coefficient) average of each line shift is the phase shift employed over the whole area.

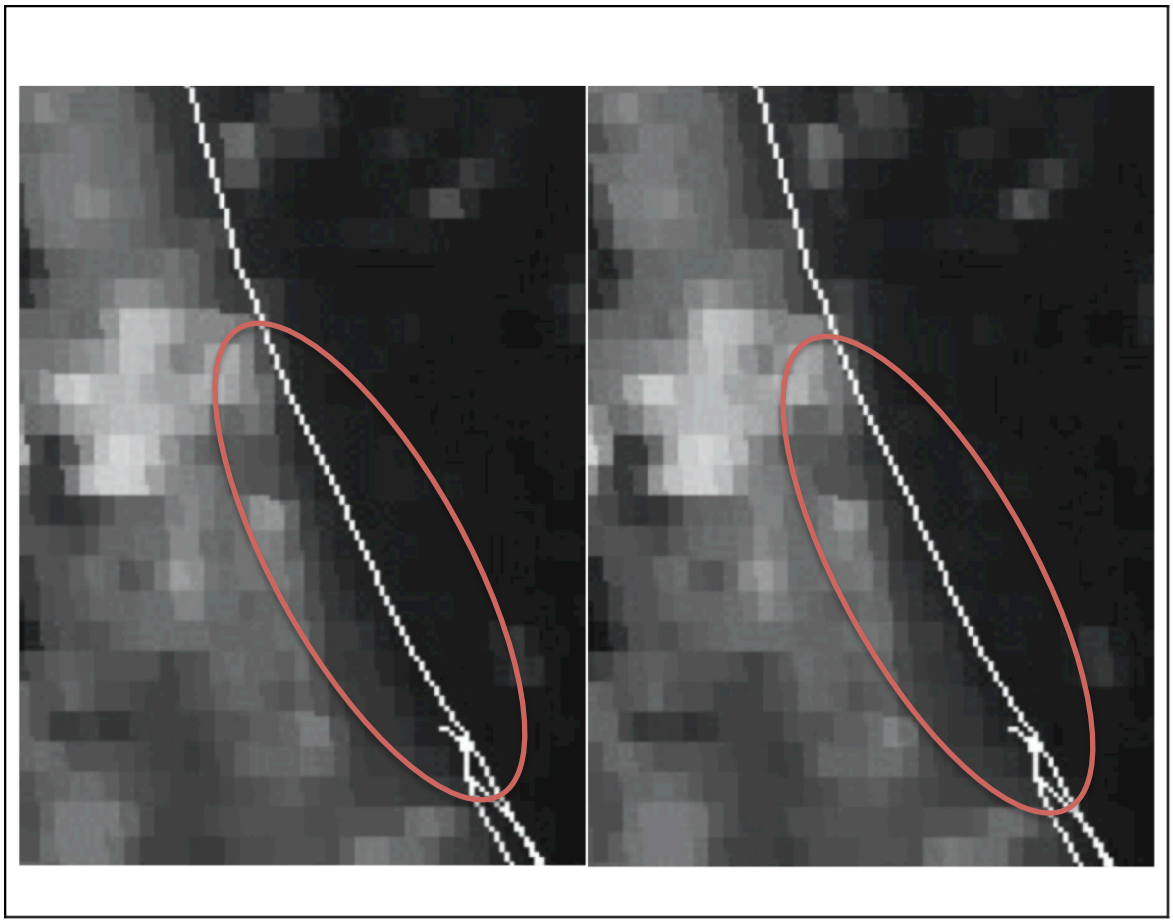

Figure E2: 3.9-μm IR imagery before correction and after correction for November 4, 2012 11:15 UTC. The original image appears to not be lined up with the eastern coastline. The FFTR algorithm calculated a co-registration error of 0.82471. The corrected image was resampled and shifted east by 0.82471 pixels.

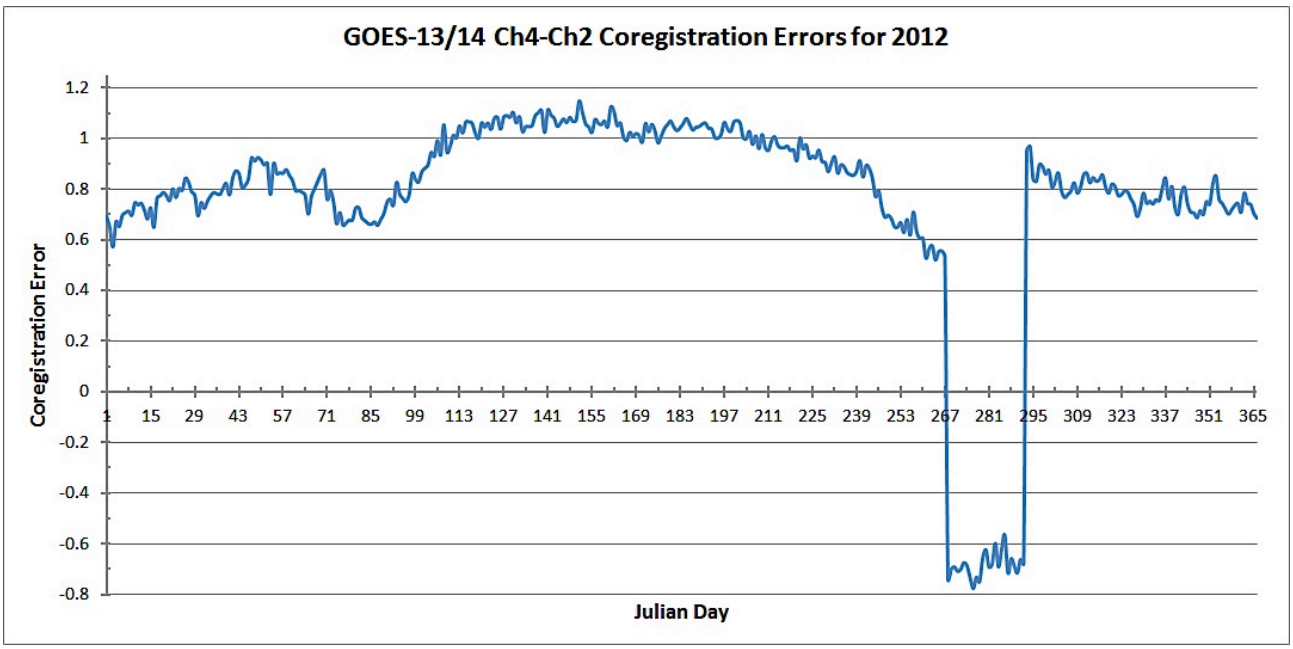

Figure E3: Shows the co-registration error that was applied to each image. The negative values reflect the GOES-14 co-registration errors.

REFERENCES

Anderson, R.K., and Coauthors, 1974: Application of meteorological satellite data in analysis and forecasting. ESSA Tech. Report NESC 51, U.S. Dept. of Commerce, Washington, DC, p. 6-B-1.

Baars, J. A., M. Witiw, and A. Al-Habash, 2003: Determining fog type in the Los Angeles basin using Historic surface observation data. *Proc. 16th Conf. on Probability and Statistics in the Atoms.* Sci., Long Beach, CA.

Bendix, J., B. Thies, J. Cermak, and T. Nauss, (2005): Ground Fog Detection from Space Based on MODIS Daytime Data - A Feasibility Study. *Wea. Forecasting*, **20,** 989-1005.

Byers, H. B., 1959: *General Meteorology* 3rd ed., McGraw-Hill, 481 pp.

Cermak, J. and J. Bendix, 2007: Dynamical nighttime fog/low stratus detection based on Meteosat Seviri data – A feasibility study. *Pure Appl. Geophys.*, **164**(6-7), 1179-1192.

Cermak, J. and J. Bendix, 2008: A novel approach to fog/low stratus detection using Meteosat 8 data. *Atmos. Res.,* **87,** 279-292.

Cermak, J., R.M. Eastman, J. Bendix, and S.G. Warren, 2009: European climatology of fog and low stratus based on geostationary satellite observations. *Quarterly Journal Royal Meteorological Society*, **135,** pp. 2125–2130.

Cermak, J., 2012: Low Clouds and Fog Along the South-Western African Coast - Satellite-Based Retrieval and Spatial Patterns, *Atmos. Res.* **116,** 15-21.

Collins, J.M., A. N. Williams, C.H. Paxton, R. J. Davis and N. M. Petro 2009: Geographical, meteorological and climatological conditions surrounding the 2008 interstate-4 disaster in Florida. Papers of the Applied Geography Conferences, 32: 153-162.

Court, A. and Gerston, R. (1966) Fog Frequency in the United States. *Geographical Review*, Vol. 56, 543-560.

Croft, Paul J., Russell L. Pfost, Jeffrey M. Medlin, G. Alan Johnson, 1997: Fog Forecasting for the Southern Region: A Conceptual Model Approach. *Wea. Forecasting*, **12**, 545–556.

Davis, G., 2007: History of the NOAA satellite program. *J. Appl. Remote Sens.*, **1,** 012504.

d'Entremont, P. ,1986: Low- and midlevel cloud analysis using nighttime multispectral imagery. *J. of Clim. And Appl. Meteor.,* **25** (12), 1853-1869,

Doswell, C. A., III, R. Davies-Jones, and D. Keller, 1990: On summary measures of skill in rare event forecasting based on contingency tables. *Wea. Forecasting*, **5,** 576-585.

Duynkerke, P.G., 1990: A comparison of model simulations with detailed observations. *Mon. Wea. Rev.* **119**, 119-324.

Eyre, J.R., J.L. Brownscombe, and R.J. Allam, 1984: Detection of fog at night using Advanced Resolution Radiometer (AVHRR) imagery. *Meteor. Mag.* **113,** 266-271.

Ellrod, G.P., 1995: Advances in the detection and analysis of fog at night using GOES multispectral infrared imager. *Wea. Forecasting.,* **10,** 606-619.

Ellrod, G.P., R.V. Achutuni, J.M. Daniels, E.M. Prins, and J. P. Nelson III, 1998: An Assessment of GOES-8 Imager Data Quality. *Bull. Amer. Meteor. Soc.*, **79**, 2509–2526.

Ellrod, G.P., 2002: Estimation of low cloud base heights at night from satellite infrared and surface temperature data. *Nat. Wea. Digest*, **26,** 39-44.

Ellrod, G.P., and S. Lindstrom, 2006: Performance of satellite fog detection techniques with major, fog-related highway accidents. *Eletronic Journal of Operational Meteorology* **2006-EJ3**

Findlater, J., 1985: Field Investigations of radiation fog formation at outstations. *Meteor. Mag.*, **114,** 187-201.

Forthun, G.M., M.B. Johnson, M.B., W.G. Schmitz, J. Blume, and R.J. Caldwell, 2006: Trends in fog frequency and duration in the southeast United States**.** *Phys. Geography*, **27,** 206–222.

Grotenhuis, M.G., X. Wu, F. Yu, T. J. Schmit, S.S. Lindstrom, and C. Cao, 2012: On-orbit characterization of the GOES Imager channel-to-channel co-registration. *Earth Observing Systems* **XVII,** Proc. SPIE 8510, 85101T.

Gultepe, I., G. Pearson, J. a. Milbrandt, B. Hansen, S. Platnick, P. Taylor, M. Gordon, J.P. Oakley, and S. G. Cober, 2008: The fog remote sensing and modeling field project. *Bulletin American Meteor. Soc*., **90**, 341-359.

Hahn, C.J., and S.G. Warren, 2007: A Gridded Climatology of Clouds over Land (1971-96) and Ocean (1954-97) from Surface Observations Worldwide. NDP-026E, Carbon Dioxide Information Analysis Center, Oak Ridge National Laboratory, Oak Ridge, TN (documentation, 71 pp.)

Hardwick, W.C. (1973) Monthly fog frequency in the continental United States. *Monthly Weather Review,* Vol. 101, 763-766.

Hillger, D. W., 1999: GOES imager and sounder calibration, scaling and image quality. NOAA Tech. Rep. NESDIS 93, 34 pp.

Houghton, D. D., 1985: *Handbook of Meteorology*, 1st ed., John Wiley and Sons, 1461 pp.

Hunt, G.E., 1973: Radiative properties of terrestrial clouds at visible and infrared thermal window wavelengths. *Quart. J. Roy. Meteor. Soc.* **99,** 346-369.

Kolb, L. L., and M. M. Goodmanson, 1945: Upslope weather along the inland Alaska air route. *J. of Meteor*. **1**, 98-108.

Lavdas, L., and G. L. Achtemeier, 1995: A fog and smoke risk index for estimating roadway visibility hazard. *National Wea Digest,* **20,** 26-33.

Lazzara, M.A., J.M. Benson, R.J. Fox, D.J. Laitsch, J.P. Rueden, D.A. Santek, D.M. Wade, T.M. Whittaker, and J.T. Young, 1999: The Man computer Interactive Data Access System: 25 Years of Interactive Processing. *Bull. Amer. Meteor. Soc.,* **80,** 271-284.

Lee, T.F., F.J. Turk and K. Richardson, 1997: Stratus and fog products using GOES-8, -9, 3.9 um data. *Wea. Forecasting,* **12**, 664-677.

Li, Zhenping, M. Grotenhuis, X. Wu, T. J. Schmit, C. Schmidt, A. J. Nelson III, F. Yu, and H. Bysal, 2014: Geostationary Operational Environmental Satellite Imager infrared channel-to-channel co-registration characterization algorithm and its implementation in the ground system. *J. Appl. Remote Sens*. 8(1), 083530.

Marzban, C. 1998: Scalar measures of performance in rare-event situations, *Wea. Forecasting*, **13,** 753-763.

Menzel, W.P., and J.F.W. Purdom, 1994: Introducing GOES-I: The first of a new generation of Geostationary Operational Environmental Satellites. *Bull. Amer. Meteor. Soc.* **75,** 757-781.

Montgomery, H.E., and L.W. Uccellini, 1985: VAS demonstration: (VISSR atmospheric sounder) description and final report. *NASA Reference Publication 1151.* National Aeronautics and Space Administration, 198 pp.

National Oceanic and Atmospheric Administration (NOAA) (1998) *Automated Surface Observing System (ASOS) User's Guide.* Retrieved November 11, 2014, from NOAA's Website at http://www.nws.noaa.gov/asos/pdfs/aum-toc.pdf

Peace, R. L. (1969) Heavy fog regions in the United States. *Monthly Weather Review*, **97,** 116-123.

Ray, P. S. , X. Du, and J. Rivard., 2014: Analysis of Prospective Systems for fog warnings. Florida Department of Transportation report number BDK83 997-19 88 pp.

Saraf, A.K., Bora, A.K., Das, J. Rawat, V., Sharma, K., and Jain, S. K. (2011) Winter fog over the Indo-Gangetic Plains: mapping and modeling using remote sensing and GIS. *Natural Hazards 201*(58), 199-220.

Schaefer, J.T., 1990: The critical success index as an indicator of warning skill. *Wea. Forecasting,* **5,** 570-575.

Schmit, T.J., M.M., Gunshor, W.P. Menzel, J.J. Gurka, J. Li, and S. Bachmeier, 2005: Introducing the next-generation baseline imager on GOES. *Bull. Amer. Meteor. Soc.,* **86**, 1079-1096.

Stull, R. B., 1999: *Meteorology for Scientists and Engineers* 2nd ed., Brooks/Cole, 502 pp.

Taylor, G., 1917: The formation of fog and mist. *Royal Meteorological Society*. **43**, 241-268.

Toth, G., I. Gultepe, J. Milbrandt, B. Hansen, G. Pearson, C. Fogarty, and W. Burrows, 2010: The Environment Canada Handbook on Fog and Fog Forecasting. *Environment Canada*, 94 pp.

Underwood, S.J., Ellrod, G.P., Kuhnert, A.L., 2004: A multiple-case analysis of nocturnal radiation-fog development off California utilizing GOES nighttime fog product. *J. Appl. Meteor.* **43,** 297-311.

Ward, B., and P.J. Croft, 2008: Use of GIS to examine winter fog occurrences. *National Weather Ass Electron J Oper. Meteorology* (EJ4):33.

Weinreb, M.P., M. Jamieson, N. Fulton, Y. Chen, J.X. Johnson, J. Bremer, C. Smith, and J. Baucom, 1997: Operational calibration of Geostationary Environmental Satellite-8 and -9 imagers and sounders," *Applied Optics*, **36**, 6895-6904.

Willett, H. C., 1928: Fog and haze, their causes, distribution and forecasting. *Mon. Wea. Rev.*,**56**, 457-468.